Modeling Friction between Shearing Brittle Surfaces with a Discrete Element Method

Master's Thesis, 2018-01-22

Author:

Sampsa Kiiskinen

Supervisors:

Timo Riikilä
Markku Kataja

UNIVERSITY OF JYVÄSKYLÄ
DEPARTMENT OF PHYSICS

Abstract

Sampsa Kiiskinen

Modeling Friction between Shearing Brittle Surfaces with a Discrete Element Method

Master's Thesis

Department of Physics, University of Jyväskylä, 2018, 76 pages

The fracture of brittle materials is a fundamental problem in material physics. It still lacks a complete theoretical description, so making predictions relies heavily on experiments and numerical models based on them. In this work we design and implement a discrete element method to study the physical system of two brittle surfaces as they are sheared across each other. Our focus is specifically how different force models for internal friction affect the dry friction of the material. By using granite as our reference material, we find that the dry friction depends strongly on the internal friction when the pressure is around the ultimate strength of the material. Otherwise the dry friction is primarily determined by the roughness of the surfaces or the thickness of the fragment layer between the them. Still, regardless of the pressure, the presence of internal friction strongly influences the mechanics inside the fragment layer.

Keywords: material physics, geophysics, computational physics, discrete element methods

Tiivistelmä

Sampsa Kiiskinen
Kitkan mallintaminen hauraiden pintojen leikkauksessa käyttäen diskreettielementtimenetelmää
Pro gradu -tutkielma
Fysiikan laitos, Jyväskylän yliopisto, 2018, 76 sivua

Hauraiden materiaalien murtuminen on eräs materiaalifysiikan peruskysymyksistä. Sille ei ole vieläkään olemassa täydellistä teoreettista selitystä, joten ennusteiden tekeminen nojaa vahvasti kokeisiin ja niihin perustuviin numeerisiin malleihin. Tässä työssä suunnittelemme ja toteutamme diskreettielementtimenetelmän sellaisen fysikaalisen systeemin tutkimiseen, jossa kaksi haurasta pintaa leikkaavat toisiaan. Keskitymme erityisesti siihen kuinka erilaiset voimamallit sisäiselle kitkalle vaikuttavat materiaalin ulkoiseen kitkaan. Käyttämällä graniittia koemateriaalina huomaamme, että sen ulkoinen kitka riippuu voimakkaasti sen sisäisestä kitkasta, kun ulkoinen paine on lähellä materiaalin puristuslujuutta. Muutoin ulkoisen kitkan määräävät pääasiallisesti leikkauspintojen karkeus tai niiden väliin muodostuneen sirpalekerroksen paksuus. Toisaalta, riippumatta ulkoisesta paineesta, sisäinen kitka vaikuttaa voimakkaasti sirpalekerroksen sisäiseen mekaniikkaan.

Avainsanat: materiaalifysiikka, geofysiikka, laskennallinen fysiikka, diskreettielementtimenetelmät

Contents

1 Introduction

To set the stage for the research question, let us briefly go over the history of friction, fracture mechanics and computational physics as they relate to it. The timeline is summarized in figure 1 for convenient reference.

1.1 Historical Context

The first recorded instance of precisely defining and experimentally measuring the coefficient of friction was done by Leonardo da Vinci around[1] the year 1500 [1]. This predated Isaac Newton's calculus and classical mechanics [2] for almost two hundred years and did not gain widespread adoption until being rediscovered by Guillaume Amontons in 1699 [3].

Over the next three hundred years several authors elaborated the foundations by considering the origins and mechanisms of friction and wear. These include the theory of adhesion by John Desaguliers in 1734 [4], the postulated microscopic origin and distinction between static and dynamic friction by Leonhard Euler in 1750 [5], the time-dependent behavior of frictional contacts by Charles-Augustin de Coulomb in 1781 [6] and the relation between rolling and sliding friction by Arthur Morin in 1832 [7]. Augmenting the models with lubrication required formulating a theory of hydrodynamic friction, which was subsequently done by Osborne Reynolds in 1886 [8] and further refined by Richard Stribeck in 1902 [9]. Although the microscopic origin of friction was examined statistically by Bowden and Tabor in 1939 [10], it took considerably longer until atomic force microscopy allowed Mate, McClelland, Erlandsson and Chiang to measure microscopic frictional forces in 1987 [11].

While people were busy coming up with new models for friction, contact mechanics began to develop as Heinrich Hertz published his 1882 work [12] on stresses inside elastic bodies in frictionless contact. This model was first extended to rigid adhesive contact by Raymond Bradley in 1932 [13] and further to elastic adhesive contact most

[1] Da Vinci never published his notebooks in a coherent manner, so this estimate is based on various incomplete collections of his early works.

notably by Johnson, Kendall and Roberts in 1971 [14], by Derjaguin, Muller and Toporov in 1975 [15] and by Carpick, Ogletree and Salmeron in 1999 [16]. Relating contact mechanics to friction was another shared effort with one of the biggest contributions being the comprehensive treatise on the theory of rolling contact by Joost Kalker in 1967 [17].

Contact mechanics is not only important for its own sake, but also because it gave rise to fracture mechanics, which is the field of study concerning what happens when the critical stress in a material is exceeded. Based on the contact mechanical analysis by Charles Inglis in 1913 [18], the paper by Alan Griffith in 1920 [19] marked the starting point of the field. Just like contact mechanics, fracture mechanics was later molded into its modern form by various authors, starting with George Irwin in 1957 [20].

As an interesting aside, there was no unifying term for the study of friction, wear and lubrication until Peter Jost started calling it tribology in his influential report in 1966 [21]. In the same time period wear also became an umbrella term for abrasion, corrosion, erosion, fatigue and fretting [22].

Shortly following the birth of fracture mechanics, the first electronic computers appeared. Together with early works like the application of the finite difference method to physical phenomena by Lewis Richardson in 1922 [23] and the theoretical exploration of both the finite difference method and the finite element method by Courant, Friedrichs and Lewy in 1928 [24] and by Richard Courant again in 1943 [25], this marked the beginning of computational physics as we know it today. In the years to come, many new numerical methods were invented. Among the most relevant ones to this work were the first prototype of molecular dynamics as published by Fermi, Pasta and Ulam in 1955 [26] and the more modern formulation of the same idea by Alder and Wainwright in 1959 [27]. Finally, the distinct element method originally proposed by Peter Cundall in 1971 [28] and later popularized by Cundall and Strack in 1979 [29] became the first member of the family of discrete element methods. Other methods such as the discrete–finite element method by Williams, Hocking and Mustoe in 1985 [30] and the discontinuous deformation analysis by Shi and Goodman in 1985 [31] soon followed.

Discrete element methods were originally intended for studying jointed rocks, which they have been very successful at [32, 33], but they have also been applied to investigate calving glaciers [34], organic agglomerates [35], synthetic ceramic–polymer

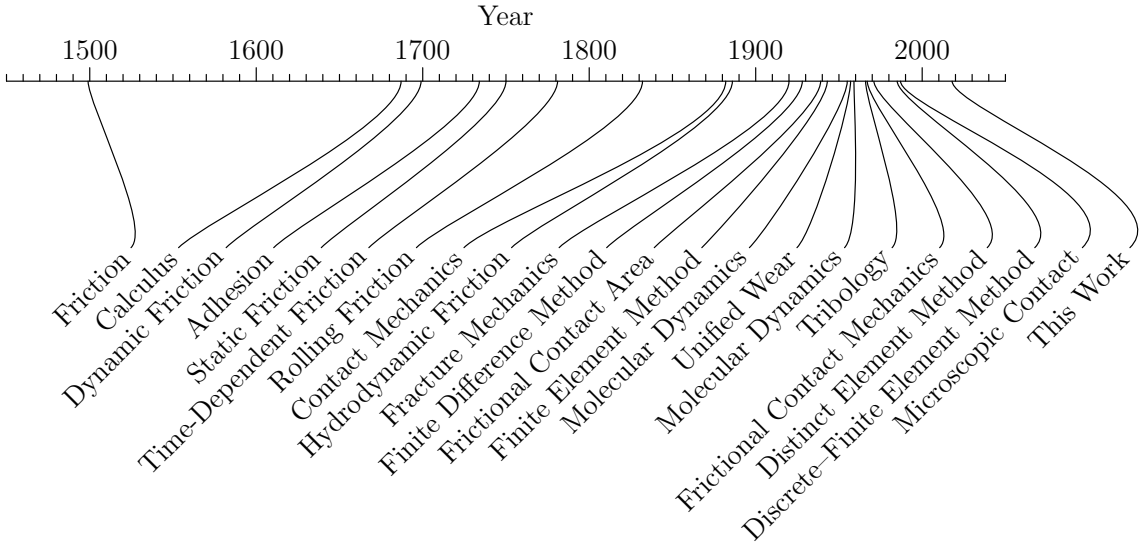

Figure 1: Timeline of selected works [1–10, 12–16, 24–26, 28, 30, 51–53] on friction, fracture mechanics and computational physics. The selection is limited by the size of the figure and based on the perceived historical importance and relevance to this work, so it is necessarily somewhat arbitrary. A more rounded view can be obtained from books [54, 55] and reviews [56, 57] solely dedicated to the subjects.

composites [36], powder flow [37] and the deformation [38], fragmentation [39], rolling [40] and piling [41] of granular media in general. Engineering applications include mill [42] and hopper [43] design, tunnel excavation [44], slope and cave stability estimation [45], pharmaceutical milling, mixing, compaction, coating, transport and storage [46] and agricultural damage estimation [47] and the processing produce [48], including oil seeds, sugar cane stems, apples, soybeans, corn, wheat, rice and rapeseed. While not directly advertised, some physics engines for video games [49, 50] are also based on discrete element methods.

In summary, friction and fracture of materials have interested physicists and engineers for centuries, but their complete theoretical description is still lacking. However, discrete element methods have been very successful at accurately predicting their behavior and, thanks to the commoditization of electronic computers, have quickly found widespread adoption.

1.2 Mission Statement

In this work we use a discrete element method to simulate the physical system of two solid surfaces as they are sheared across each other. The surfaces are made of the same material, which is[2] amorphous, isotropic and brittle. The time development of the system consists of four distinct phases that are displayed in figure 2.

The system itself has been studied before, both theoretically [58, 59] and experimentally [60, 61], but always with a specific model in mind. The goal here is to instead explore the design space of simulations by comparing the effects various models for internal friction have on the resulting dry friction. This should shed light on the appropriate choice of force models and their calibration, both of which are difficult problems in the general case [62, 63].

For this work we choose granite as a reference material, because it is suitably brittle, familiar from everyday life, easily available for experiments and has well-known physical properties. It is also easier to be confident in the validity of the model if it is not needlessly abstract.

1.3 Relation to Other Fields

In geophysics parlance, our system would be called a fault, making the shearing represent an earthquake. The fragmentation would be dubbed comminution and the resulting layers of fragments would be classified as cataclastic rocks. The rocks themselves would either be breccia or gouge, depending on the fragment size distribution. With this terminology in mind, the research question would be loosely related to a problem known as the heat flow paradox, which concerns the unexpected lack of frictional heating in the San Andreas fault [64].

Condensed matter physics is at the other end of the length scale, but features similar concepts. If our particles were molecules, the system would resemble a sedimented colloidal suspension. Quantized elastic waves in the material would be called phonons and variations in its particle size distribution would be referred to as its dispersity. This is a useful connection to make, because some statistical results from condensed matter physics [65] can be used in this work as well.

[2] These terms mean that the material is not crystalline, looks the same in all directions and fails suddenly after elastic deformation.

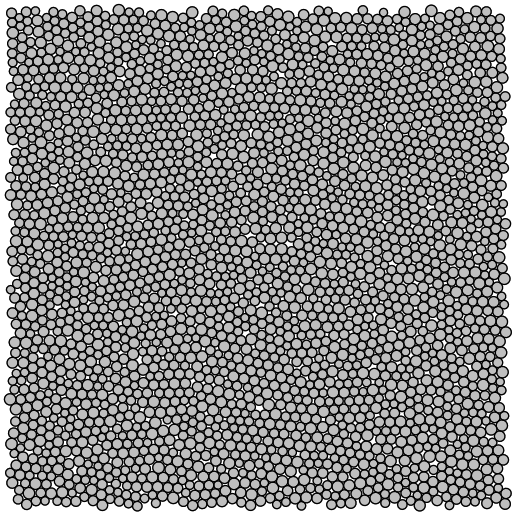

(a) A block of material is formed by packing loose particles together.

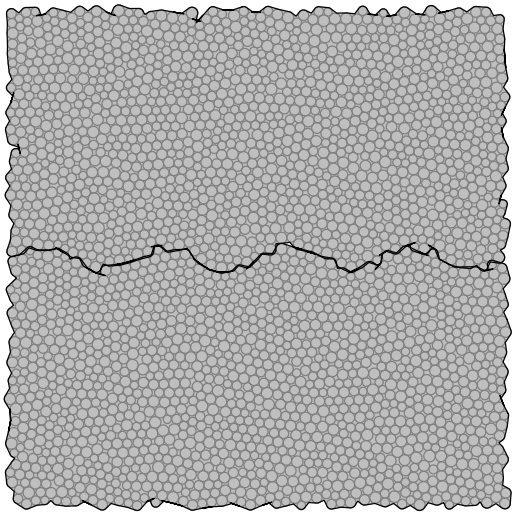

(b) The block is artificially split into two halves and pulled apart slightly to create a fault.

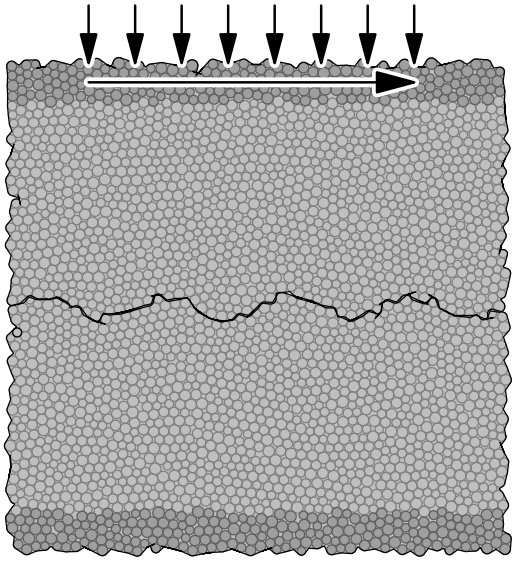

(c) The edge of one half is held in place as a horizontal driving force is applied to the edge of the other half under a constant vertical pressure.

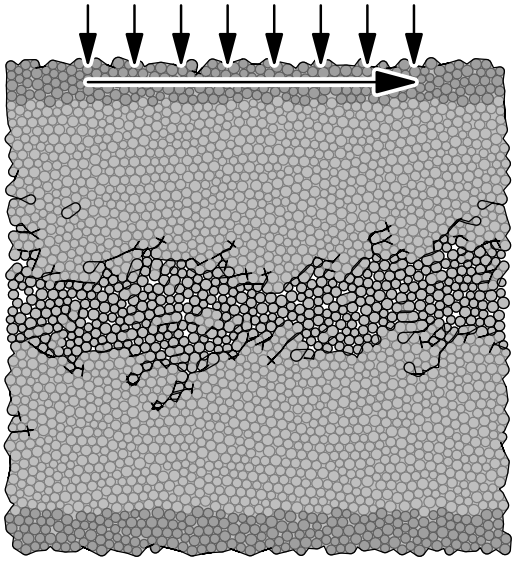

(d) The horizontal force and vertical pressure are maintained until enough fragments have appeared to make meaningful measurements.

Figure 2: Sketches of the physical system of interest. The system extends to infinity in the direction of the shearing through periodic boundary conditions.

2 Basic Concepts

In this section we introduce the foundational concepts needed to understand the research question and motivate some of the problems therein. The structure of the rest of this work is also laid out at the end of this section.

2.1 Microscopic and Macroscopic Friction

Friction refers to dissipative forces that resist the relative motion of surfaces, whether the surfaces are interfaces between materials or layers within the same material. It is not a fundamental force but rather an idealized statistical classification of microscopic forces that are complicated enough to make it infeasible to derive from first principles.

Friction is commonly divided into different kinds based on the context it appears in. In this work we talk about

dry friction, which describes the tendency of macroscopic solid objects in contact to oppose sliding across each other,

internal friction, which can be thought of as the microscopic constituents of a plastic or viscoelastic material resisting deformation, and

fluid friction, which manifests as flow resistance in purely viscous materials.

If the behavior at rest differs from that in motion, the kinds are further divided into

static friction, which appears when the surfaces have been at rest long enough for them to jam or bond together weakly, and

dynamic friction, which is exactly the opposite.

Since dry friction and dynamic friction are often referred to as just friction, fluid friction and static friction may be called viscosity and stiction [66] respectively to emphasize the difference.

The simplest model for dry friction is Amontons' law, which states that the frictional force

$$F^{\mathrm{t}} = \mu F^{\mathrm{n}}, \tag{1}$$

where F^{n} is the loading force and μ is a constant called[3] the coefficient of friction. The coefficient of friction is a property of the physical system, depending primarily on the materials of the contacting surfaces and secondarily on a slew of other factors such as the external loading configuration [67]. For most systems $0 < \mu < 1$, although contacts with sticky materials like rubber may have $\mu \geq 1$ and adhesive and nanoscale systems [68] can exhibit $\mu < 0$. As an example, granite in contact with itself has $\mu \approx 0.7$ [69].

For internal friction in a solid, one of the simplest models is the Kelvin–Voigt model, which states that

$$\sigma = Y\varepsilon + \eta_G \partial_t \varepsilon, \tag{2}$$

where σ is stress, ε is strain, t is time, Y is the Young's modulus of the material and η_G is its dynamic viscosity. The idea behind this model is to describe the material as a spring with stiffness Y and a dashpot with sluggishness η_G, both ideal and connected in parallel. Without the dashpot, the material would be perfectly elastic and there would be no friction involved. Coming back to the previous example, this model suits granite at long time scales with $Y \approx 50\,\mathrm{GPa}$ [70] and $\eta_G \approx 50\,\mathrm{EPa\,s}$ [71].

While the model in equation 1 is very crude, it works well for characterizing both the static and dynamic friction of rigid bodies and makes comparing systems a simple matter of comparing their coefficients of friction. Similarly, the model in equation 2 is a decent way to characterize creep in solid materials for only relying on two material parameters. Alas, both of these models and their more advanced counterparts are based on the assumption that the material is elastic and forms a continuum. As soon as there is plastic deformation or fracture, the models become little more than useless. Even if this was not the case and the models worked fine in isolation, there is no universal way to combine them, because they work at vastly different length scales.

[3]The notational conventions are summarized in appendix section A.

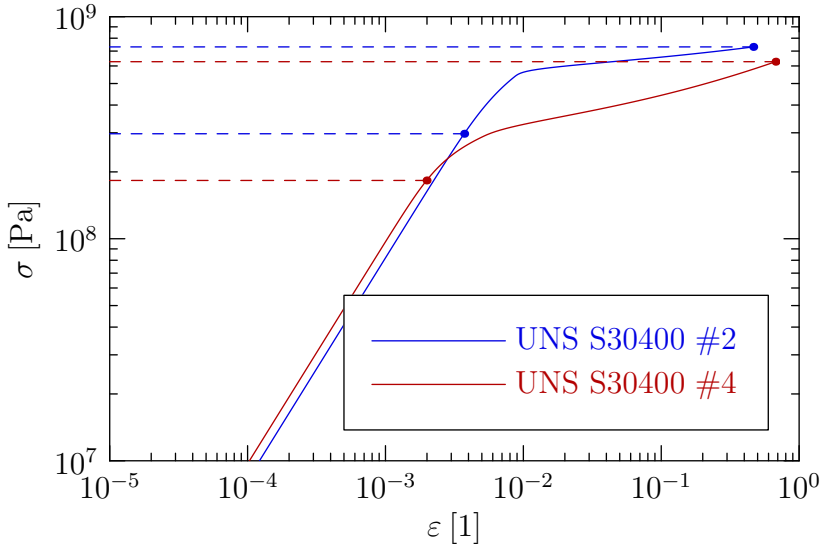

Figure 3: Tensile stress σ as a function of strain ε for two stainless steel samples [72]. As expected of a ductile material, the yield strength is substantially smaller than the ultimate strength, both of which are marked on the curves. See figure 4 for a comparison with granite.

2.2 Deformation and Fragmentation

Whenever a solid material is subjected to a sufficiently large stress, it will undergo irreversible plastic deformation or fracture. The stress corresponding to the onset of these changes is called the yield strength and the stress at which fracture finally happens is called the ultimate strength. For many materials the yield strength is smaller than the ultimate strength, resulting in gradual failure preceded by observable changes in the material. For brittle materials, however, the ultimate strength is very close to the yield strength, making failure sudden and unpredictable. This difference is demonstrated for stainless steel and granite in figures 3 and 4 respectively.

A material may also respond differently to compressive and tensile stresses. It is common to work with the assumption that the responses are equal, but this assumption is generally unfounded for processes involving large stresses. This is apparent in figure 4, where the ultimate tensile strength $\sigma^{\text{crit n}} \approx 20\,\text{MPa}$ is an order of magnitude smaller than the ultimate compressive strength $\sigma^{\text{crit n}} \approx 280\,\text{MPa}$. Composite materials like reinforced concrete exist to balance these properties.

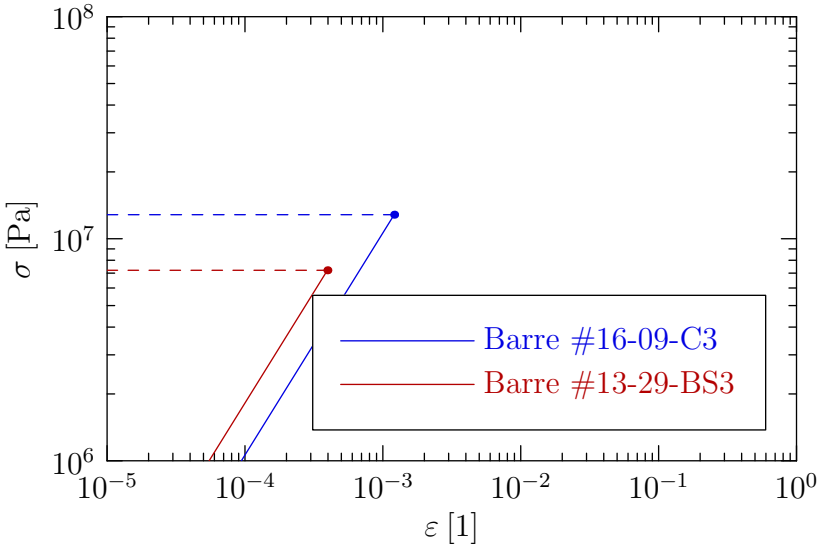

Figure 4: Tensile stress σ as a function of strain ε for two granite samples [70]. As expected of a brittle material, the yield strength coincides with the ultimate strength, which is marked on the curves. See figure 3 for a comparison with stainless steel.

2.3 Discrete Element Methods

Discrete element methods (henceforth DEM in both singular and plural) are, as the name suggests, numerical simulation methods featuring a finite number of distinguishable particles. In DEM, the system of interest is constructed from suitably composed particles and time is advanced by moving said particles according to the laws of classical mechanics. Precisely how the particles are composed and how time is advanced varies from method to method, but the most popular choice is spherical particles with either force-based or event-driven time development.

To give some perspective, DEM are very similar to molecular dynamics (MD) with the exception that particles may have more degrees of freedom, assume more complicated shapes, feature time-dependent interaction mechanisms and bear some internal structure. Indeed, the original distinct element method [29] was basically two-dimensional force-based MD with additional rotational degrees of freedom and short-range contact forces in place of long-range electromagnetic forces. From another point of view, DEM resemble finite element methods (FEM), where the vertices of the mesh may move, the local topology of the mesh may vary, the ambient space of the mesh may only be covered partially and the boundaries of the mesh may change.

This connection to FEM may seem like a stretch, but it is roughly how the theory of the discrete–finite element method [30] was first formulated.

One of the major benefits DEM have over other simulation methods and even theoretical approaches is their ability to model fragmentation. Since fragmentation in real materials emerges from the way their constituents interact with each other, mimicking these interactions in DEM produces qualitatively correct behavior without having to involve fracture mechanics. Other benefits include how easy DEM are to understand conceptually, how conveniently their implementations scale and parallelize and how implementing them does not require generating or performing operations on triangular meshes, because having to do so is unwieldy and known to create nonphysical artifacts in some applications [63].

Nevertheless, DEM are far from the ultimate solution to every problem as calibrating them to match experiments is tricky, applying them to large systems and long runs require a lot of processing power and implementing them efficiently is laborious and complicated. There is also considerably less established software infrastructure for DEM than for MD or FEM.

Understanding DEM in detail is best done constructively by considering the process of making one. We divide this process into design and implementation phases as shown in figures 5 and 6 respectively. The motivation for the division is that the design phase is primarily carried out with pen and paper while the implementation phase is more heavy on programming. In this work the design phase leads us to differently sized spheres in two dimensions with force-based time development and breaking under tensile and compressive stresses. The implementation, on the other hand, ends up being written in[4] the C programming language. We walk through these choices in the sections to come.

[4]The code follows the modern standards ISO/IEC 9899:2011 and POSIX.1-2008.

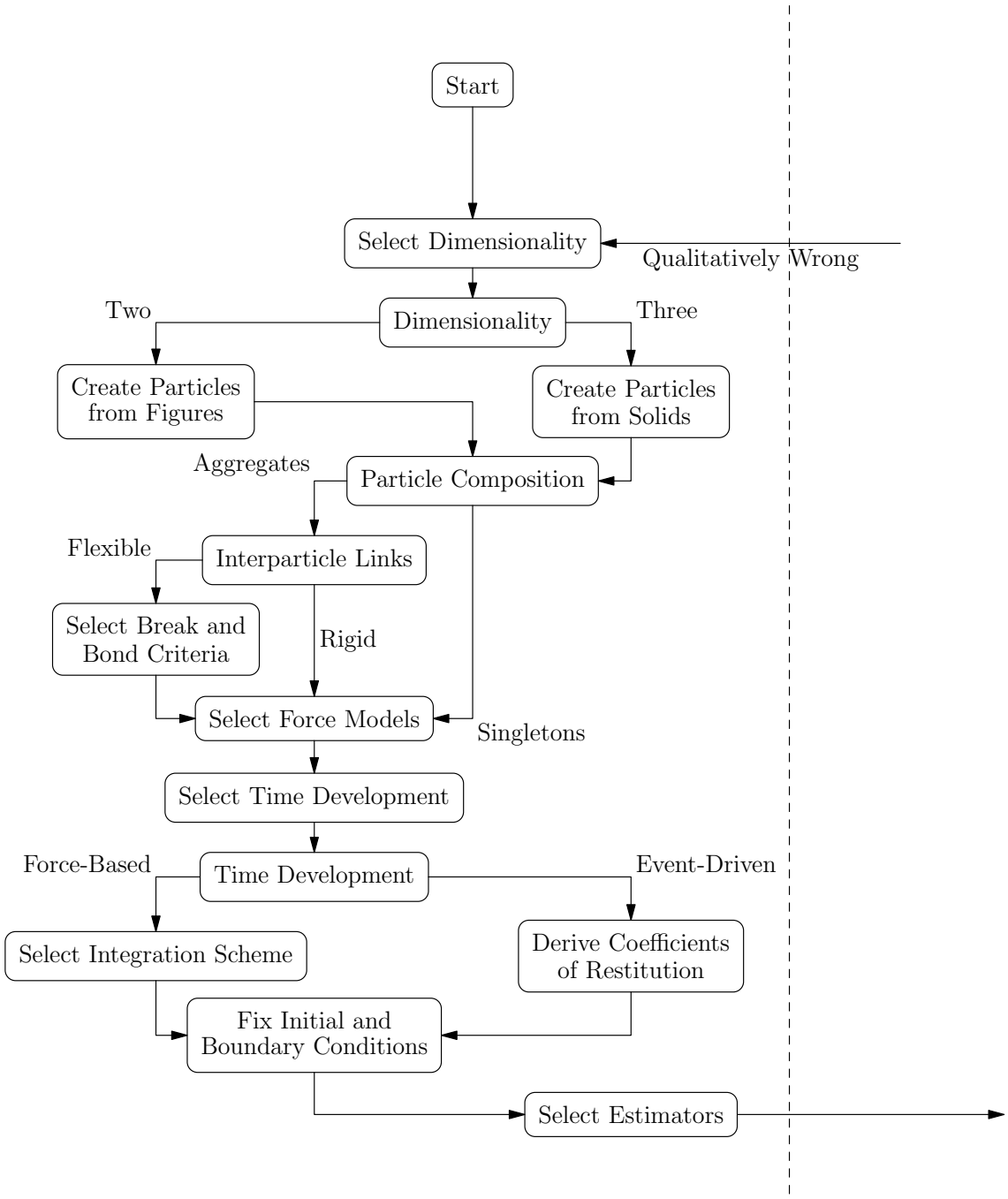

Figure 5: Flowchart of the design phase of a DEM. See figure 6 for the implementation phase.

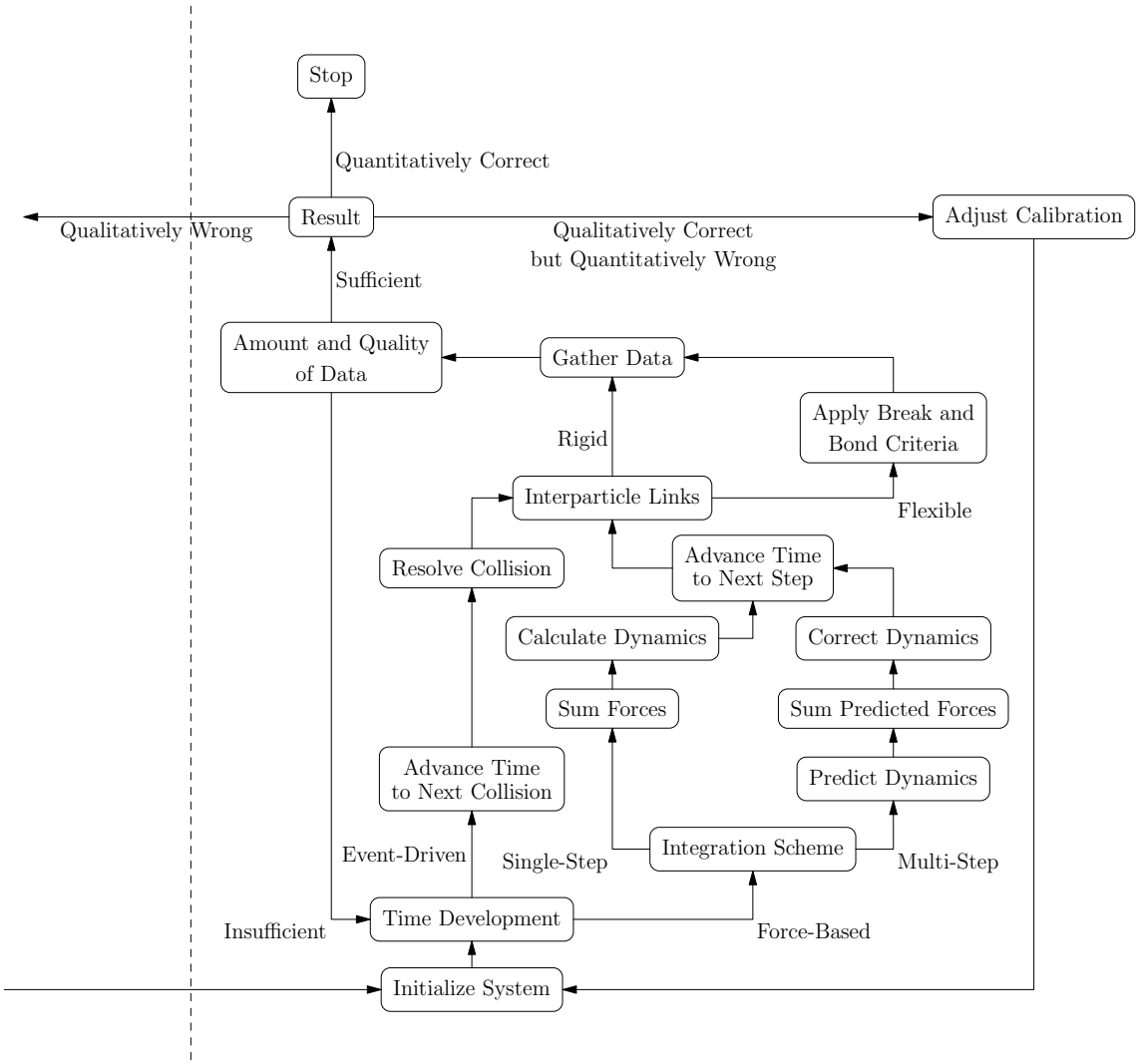

Figure 6: Flowchart of the implementation phase of a DEM. See figure 5 for the design phase.

3 Theoretical Design

Our focus in this section is the theory needed for designing the simulation. We try to be careful with the details, such as repulsive forces always having negative signs, to help the reader who might want to implement the simulation.

3.1 Dimensionality

If the isotropic block of material we started with formed a continuum, the system would be completely symmetric in all directions. Introducing a fault and a driving force would then break the symmetry in two directions, but the system would still be symmetric along the intersection line of the fault plane and the plane perpendicular to the driving force vector. Due to the remaining symmetry, we could completely describe the system in two dimensions.

In reality the block of material is made of finitely sized particles, so it does not form a continuum and, as a consequence, the fault is not exactly a plane. The practical consequence of this is that the driving force may actually move particles in any direction within the fault. The movement in the direction of the assumed symmetry should, however, be statistically insignificant for the measurements we are interested in, so we ignore it.

These mental contortions to justify the use of two dimensions are not without merit. Assuming the characteristic side length of the system is L and the characteristic radius of the particles is R, going from three dimensions to two dimensions scales the number of particles required in the worst case[5] by $N_3/N_2 = (\sqrt{6}/4)(L/R)$. In the case of a 100 mm block made of 2 mm particles, this comes out as $N_3/N_2 \approx 61$. The change from three dimensions to two dimensions also reduces the degrees of freedom[6] per particle from $3+3$ to $2+1$ and the maximum number of contacts per particle (the kissing number) from 12 to 6. This is notable, because contact calculations scale quadratically[7] with respect to the number of neighboring particles, so we drop from

[5] The dependence is derived in appendix section B.

[6] The notation here is $T+R$ for T translational and R rotational degrees of freedom.

[7] The requirements of contact calculations are elaborated in section 4.4.1.

66 to 15 contact calculations per particle in the worst case.

One more thing to consider is the mapping between our two-dimensional system and three-dimensional reality. When we construct the two-dimensional system, we merely constrain the dynamics of three-dimensional particles into two dimensions. Treating the system as a three-dimensional extrusion of a two-dimensional profile would not work well with models that were originally derived for three-dimensional geometries [73].

3.2 Particle Composition

Particle composition refers to the shapes of the smallest indivisible particles and the ways they are linked together. The appropriate choice for both features is a compromise between simplicity and realism, just like in the case of dimensionality.

The most popular choices for the shapes are discs or spheres, because their collision detection does not depend on their angular displacements and their interactions can be derived directly from contact mechanics [74]. Other popular choices are polygons or polyhedra, because they can be decomposed into triangles or tetrahedra and handled by case analysis [75].

When links are introduced, they can either be completely rigid or somewhat flexible. The main purpose of rigid links is building more complicated shapes out of the few basic ones without having to devise new collision detection algorithms. Flexible links, on the other hand, are far more versatile. When taken to behave like springs or beams, they allow the modeling of properties like deformation or fracture. While using flexible links is not the only way to model either property, no other approach quite compares in the breadth of literature and variety of models to choose from [62, 76–78].

In this work we employ spheres with two kinds of flexible links. Strong links represent covalently bond regions and as such keep intact blocks of solid material together. They are made of viscoelastic beams that break under sufficient stress. Weak links represent van der Waals forces and appear in contact interactions of loose particles. They form when particles come into contact and vanish as soon as the particles depart. The whole arrangement is fictitious in the sense that it does not accurately represent the microscopic structure of the material it makes up, but that is fine as long as it behaves as if that was the case.

These choices allow the efficient implementation of many types of forces, but not

without their own set of problems. The biggest concern is the distinct lack of surface geometry in the spheres, which means that certain properties, such as static friction, need to be included in the force models in an inelegant and physically questionable manner. This is not merely an aesthetic issue, but also makes calibration harder, because it tends to give rise to physically meaningless parameters that cannot be derived directly from theory or experiments.

3.3 Interactions

We consider the interactions of pairs of particles with each other and the influence of external or ambient forces on single particles separately. While there are situations where multi-body interactions arise[8] from the limitations of the model, we do not have to worry about them due to our time development[9] being force-based and the effect of high-speed collisions being negligible.

3.3.1 Pair Interactions

When modeling the collision of two indivisible particles, we consider them to be completely rigid, but allow them to overlap each other. The overlapping is taken to imply deformation, whereas wear is purposefully neglected. This concept is illustrated in figure 7, along with the variables that we need to define.

Our starting point is the usual Euclidean space with 2 dimensions, where the laboratory frame of reference consists of the right-handed Cartesian coordinate system centered at the origin and spanned by the basis vectors $\vec{e}^{\mathrm{x}}$ and $\vec{e}^{\mathrm{y}}$. The space is inhabited by N distinguishable particles, each of which is a rigid sphere with a homogenous mass distribution and open boundary. Given a particle indexed with i, it has the radius r_i and mass m_i and, at each point in time t, has the displacement $\vec{x}_i(t)$, velocity $\vec{v}_i(t)$, acceleration $\vec{a}_i(t)$, angular displacement $\varphi_i(t)$, angular velocity $\omega_i(t)$ and angular acceleration $\alpha_i(t)$. To avoid clutter, we forgo writing the time parameter explicitly when referring to the current point in time t.

We establish another frame of reference for each pair of particles. Given two different particles indexed with i and j, their pair frame is just like the laboratory frame, except that it is centered at the focal point $\vec{o}_{i,j}$ and spanned by the normal

[8] Simulating a Newton's cradle with event-driven time development is a good example, since naive collision resolution would have problems keeping the balls in the middle at rest.

[9] The choice of time development is discussed more in section 3.6.

and tangential basis vectors $\vec{e}^{\,\mathrm{n}}_{i,j}$ and $\vec{e}^{\,\mathrm{t}}_{i,j}$ respectively. The focal point is defined as the intersection point of the collinear and radical axes of the particles, as in

$$\vec{o}_{i,j} = \vec{x}_i + b_{i,j}(\vec{x}_j - \vec{x}_i) = \vec{o}_{j,i}, \tag{3}$$

where the overlap factor

$$\begin{aligned} b_{i,j} &= \frac{1}{2}\begin{cases} 1 - (r_j^2 - r_i^2)/|\vec{x}_j - \vec{x}_i|^2, & \vec{x}_i \neq \vec{x}_j \\ 1, & \vec{x}_i = \vec{x}_j \end{cases} \\ &= 1 - b_{j,i}. \end{aligned} \tag{4}$$

This is a convenient definition, because when the particles overlap, the focal point corresponds to the center of the contact, and when they do not, it corresponds to the midpoint of their tangents, which is where a link between them would be. The basis vectors follow the same line of reasoning. The normal vector is defined as the unit vector from i to j and is thus parallel to the collinear axis. The tangent vector is defined as its right-handed perpendicular and is therefore parallel to the radical axis. In other words

$$\vec{e}^{\,\mathrm{n}}_{i,j} = \frac{\vec{x}_j - \vec{x}_i}{|\vec{x}_j - \vec{x}_i|} = -\vec{e}^{\,\mathrm{n}}_{j,i} \qquad\qquad \vec{e}^{\,\mathrm{t}}_{i,j} = \operatorname{per} \vec{e}^{\,\mathrm{n}}_{i,j} = -\vec{e}^{\,\mathrm{t}}_{j,i}, \tag{5}$$

where per is[10] the right-handed vector perpendicularization function.

We can now write the force exerted by j on i as

$$\vec{F}_{i,j} = \vec{F}^{\,\mathrm{n}}_{i,j} + \vec{F}^{\,\mathrm{t}}_{i,j} = F^{\mathrm{n}}_{i,j}\vec{e}^{\,\mathrm{n}}_{i,j} + F^{\mathrm{t}}_{i,j}\vec{e}^{\,\mathrm{t}}_{i,j} = -\vec{F}_{j,i}, \tag{6}$$

where both the normal component $F^{\mathrm{n}}_{i,j}$ and the tangential component $F^{\mathrm{t}}_{i,j}$ depend on the choice of the force models. Since there is a tangential component, the force also induces the torque

$$\tau_{i,j} = d_{i,j} F^{\mathrm{t}}_{i,j}, \tag{7}$$

where $d_{i,j}$ is the distance from the assumed[11] contact point.

[10] An explicit definition for per is given in appendix section C.

[11] The contact point assumption is discussed in appendix section D.

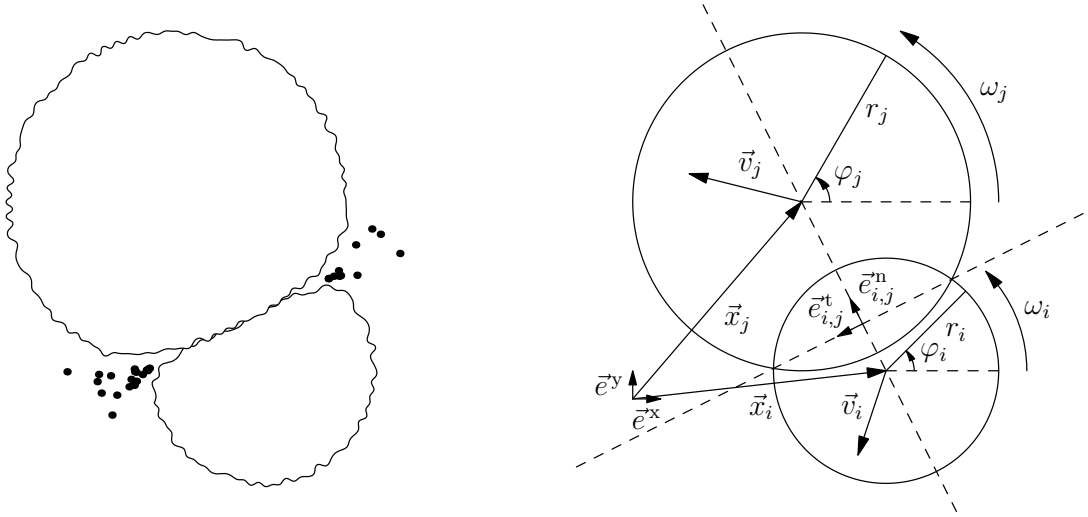

(a) In reality particles have rough surfaces and, upon colliding with other particles, may experience significant deformation and wear.

(b) In our model particles are completely rigid spheres and, instead of colliding with other particles, may come to overlap them. The variables are defined in section 3.3.1.

Figure 7: Contrasting the model for pair interactions with reality.

3.3.2 External Potential

In addition to pair interactions, there may be an external potential U, which each particle i experiences via the conservative force field

$$\vec{F}_i^{\,\mathrm{ext}} = -\vec{\nabla} U_i. \tag{8}$$

The potential generally induces a torque as well, but not for spherical bodies with constant density, so we may safely assume that

$$\tau_i^{\,\mathrm{ext}} = 0. \tag{9}$$

Conservative force fields arise naturally from phenomena like gravity, which we could model with the potential

$$U_i = a^{\,\mathrm{ext}} m_i x_i^{\,\mathrm{y}}, \tag{10}$$

where $a^{\,\mathrm{ext}}$ is the magnitude of the gravitational acceleration in the direction of $-\vec{e}^{\,\mathrm{y}}$. Aside from gravity, external potentials are also useful for artificially controlling

the system. One example of this is the harmonic potential we use for packing the particles together when forming the initial block[12] of material.

3.3.3 Ambient Forces

It is sometimes desirable to model friction in the surrounding media or to damp vibrations in excessively elastic regions of the system [58]. This requires an ambient and dissipative force field, which cannot be created through pair interactions or external potentials alone.

The drag force [79] experienced by particle i in isolation is

$$\vec{F}^{\,\mathrm{amb}} = -\frac{1}{2}\rho^{\,\mathrm{amb}} A_i C_i |\vec{v}_i| \vec{v}_i, \tag{11}$$

where $\rho^{\,\mathrm{amb}}$ is the density of the surrounding media, A_i is the cross-sectional area of the particle and C_i is a dimensionless number known as the drag coefficient. Since the particle is spherical, we can write A_i and C_i in terms of the radius r_i and the Reynolds number

$$\mathrm{Re}_i = 2\left(\frac{\rho^{\,\mathrm{amb}}}{\eta_G^{\mathrm{amb}}}\right) r_i |\vec{v}_i|, \tag{12}$$

where η_G^{amb} is the dynamic viscosity of the surrounding media. This results in

$$A_i = \frac{(2\pi)}{2} r_i^2 \tag{13}$$

and, according to an experimental correlation [80] that should be accurate enough for our purposes,

$$C_i = \frac{8}{\mathrm{Re}_i \sqrt{\Phi_\parallel}} + \frac{16}{\mathrm{Re}_i \sqrt{\Phi_\circ}} + \frac{3}{\sqrt{\mathrm{Re}_i \sqrt{\Phi_\circ^3}}} + \frac{D_1^{D_2(-\log \Phi_\circ)^{D_3}}}{\Phi_\perp}, \tag{14}$$

where the particle sphericities $\Phi_\circ = \Phi_\perp = \Phi_\parallel = 1$ and

$$D = \begin{bmatrix} 4.21 \cdot 10^{-1} \\ 4.00 \cdot 10^{-1} \\ 2.00 \cdot 10^{-1} \end{bmatrix}. \tag{15}$$

With these considerations, the drag force

$$\vec{F}_i^{\,\mathrm{amb}} = -\frac{(2\pi)}{16}\left(\frac{(\eta_G^{\mathrm{amb}})^2}{\rho^{\,\mathrm{amb}}}\right)\left(\frac{24}{\mathrm{Re}_i} + \frac{3}{\sqrt{\mathrm{Re}_i}} + 1\right) \mathrm{Re}_i^2 \, \frac{\vec{v}_i}{|\vec{v}_i|}. \tag{16}$$

[12] Initial conditions are discussed more in section 3.7.3.

If portraying the surrounding media accurately is not particularly important or the Reynolds number roughly satifies $\mathrm{Re}_i < 1$, we can simplify things considerably by assuming creeping flow. For creeping flow the drag coefficient only consists of the first term

$$C_i = \frac{24}{\mathrm{Re}_i}, \tag{17}$$

which makes the drag force

$$\vec{F}_i^{\,\mathrm{amb}} = -3\,(2\pi)\,\eta_G^{\mathrm{amb}} r_i \vec{v}_i \tag{18}$$

and the corresponding torque

$$\tau_i^{\mathrm{amb}} = -4\,(2\pi)\,\eta_G^{\mathrm{amb}} r_i^3 \omega_i. \tag{19}$$

These equations are equivalent to Faxén's laws [81], but without the disturbance terms that would appear if we considered the effects particles have on each other.

3.3.4 Driving Force

With just the natural interactions in play, our system would eventually settle to an equilibrium position. In order to maintain the shearing motion indefinitely, we have to introduce a driving force that does enough work to balance the energy dissipation.

We define the driving force for each particle i such that

$$\vec{F}_i^{\,\mathrm{driv}} = \delta_i^{\mathrm{driv}} (F_i^{\mathrm{driv\,x}} \vec{e}_i^{\,\mathrm{x}} + F_i^{\mathrm{driv\,y}} \vec{e}_i^{\,\mathrm{y}}), \tag{20}$$

where $\delta^{\,\mathrm{driv}}$ is an indicator[13] for being driven, the number of driven particles

$$N^{\,\mathrm{driv}} = \sum_i \delta_i^{\mathrm{driv}} \tag{21}$$

and the components $F_i^{\mathrm{driv\,x}}$ and $F_i^{\mathrm{driv\,y}}$ are adjusted to fulfill

$$\begin{aligned} \frac{1}{N^{\,\mathrm{driv}}} \sum_i \delta_i^{\mathrm{driv}} v_i^{\mathrm{x}} &= v^{\,\mathrm{driv}} \\ \frac{1}{N^{\,\mathrm{driv}}} \sum_i \delta_i^{\mathrm{driv}} \frac{F_i^{\mathrm{driv\,y}}}{A^{\mathrm{y}}} &= p^{\,\mathrm{driv}}, \end{aligned} \tag{22}$$

[13] We have $\delta_i^{\mathrm{driv}} = 1$ if particle i is driven and $\delta_i^{\mathrm{driv}} = 0$ if it is not.

where v^{driv} is the horizontal target speed, p^{driv} is the vertical target pressure and A^{y} is the area of the driven surface. In three dimensions the area would simply be

$$A^{\mathrm{y}} = l^{\mathrm{x}} l^{\mathrm{z}}, \tag{23}$$

where l are the side lengths of the system, but there is no such thing as depth in two dimensions, so l^{z} does not exist. To settle this problem, we observe that since the initial block[14] of material is supposed to be isotropic, we could form it by stacking together suitable two-dimensional slices some characteristic length L^{z} apart. This means that we can write

$$A^{\mathrm{y}} = l^{\mathrm{x}} L^{\mathrm{z}}, \tag{24}$$

where the characteristic length

$$L^{\mathrm{z}} = \frac{2}{N} \sum_i r_i \tag{25}$$

follows from the particle size distribution.

3.3.5 Summary of Interactions

Since pair interactions, external potentials and ambient forces are independent of each other, each particle i is subjected to the total force

$$\begin{aligned} \vec{F}_i &= \sum_j^{j \neq i} \vec{F}_{i,j} - \vec{\nabla} U_i + \vec{F}_i^{\,\mathrm{amb}} + \vec{F}_i^{\,\mathrm{driv}} \\ &= \sum_j^{j \neq i} (F_{i,j}^{\mathrm{n}} \vec{e}_{i,j}^{\,\mathrm{n}} + F_{i,j}^{\mathrm{t}} \vec{e}_{i,j}^{\,\mathrm{t}}) - \vec{\nabla} U_i + \vec{F}_i^{\,\mathrm{amb}} + \delta_i^{\mathrm{driv}} (F_i^{\mathrm{driv\,x}} \vec{e}_i^{\,\mathrm{x}} + F_i^{\mathrm{driv\,y}} \vec{e}_i^{\,\mathrm{y}}) \end{aligned} \tag{26}$$

and torque

$$\tau_i = \sum_j^{j \neq i} \tau_{i,j} + \tau_i^{\mathrm{amb}} = \sum_j^{j \neq i} d_{i,j} F_{i,j}^{\mathrm{t}} + \tau_i^{\mathrm{amb}}, \tag{27}$$

where $F_{i,j}^{\mathrm{n}}$, $F_{i,j}^{\mathrm{t}}$, $d_{i,j}$, U_i, $\vec{F}_i^{\,\mathrm{amb}}$ and τ_i^{amb} depend on the choice of the force models.

[14] Initial conditions are discussed more in section 3.7.3.

3.4 Force Models

Whether time development is force-based or event-driven, all interactions come down to the definition of the forces, which is why choosing the appropriate force models is at the crux of this work. Luckily there is no shortage of models to choose from. Even a short literature review reveals six options for normal forces and another six for tangential forces [62, 78], each of which can be calibrated to fit the task at hand.

3.4.1 Normal and Tangential Displacements

Whenever two different particles i and j interact, their interaction can be characterized by the normal displacement $\xi_{i,j}$ and tangential displacement $\zeta_{i,j}$. The normal displacement represents the relative movement of the particles along $\vec{e}^{\,\mathrm{n}}_{i,j}$ and has a positive value if they overlap. It is easy to derive and ends up being exactly

$$\xi_{i,j} = (r_i + r_j) - |\vec{x}_j - \vec{x}_i| = \xi_{j,i}. \tag{28}$$

The tangential displacement is similar to the normal displacement, except it goes along $\vec{e}^{\,\mathrm{t}}_{i,j}$ and is somewhat trickier to derive.

Looking at the pair frame of i and j, the angle of the frame itself in the laboratory frame is

$$\lambda_{i,j} = \arctan \vec{e}^{\,\mathrm{n}}_{i,j} = \operatorname{rev} \lambda_{j,i}, \tag{29}$$

where rev is[15] the angle reversal function. The angular displacement of particle i in the pair frame is thus

$$\psi_{i,j} = \varphi_i - \lambda_{i,j}. \tag{30}$$

If the particles initiate their interaction at some point in time $t^{\mathrm{init}}_{i,j}$, the angular displacement of i is the difference

$$\Delta\psi_{i,j} = \psi_{i,j} - \psi_{i,j}(t^{\mathrm{init}}_{i,j}) \tag{31}$$

and the tangential displacement ends up being approximately

$$\zeta_{i,j} = d_{i,j}\Delta\psi_{i,j}, \tag{32}$$

[15] An explicit definition for rev is given in appendix section C.

where, again, $d_{i,j}$ is the distance from the assumed[16] contact point.

In addition to the normal and tangential displacements, we introduce the adjusted normal displacement

$$\Xi_{i,j} = \Big(d_{i,j}(t_{i,j}^{\text{init}}) + d_{j,i}(t_{i,j}^{\text{init}})\Big) - |\vec{x}_j - \vec{x}_i| = \Xi_{j,i}, \tag{33}$$

which is relative to the initial distance between the particles instead of being relative to their radii. The adjustment makes the normal displacement more consistent with the tangential displacement and helps avoid the creation of stresses in the material when bonding particles together.

To describe elastic behavior in force equations, we may use any combination of the normal and tangential displacements directly. However, to describe viscous behavior, we also need their rates of change. This can be accomplished through straightforward differentiation, which produces the normal and tangential velocities

$$\begin{aligned} \partial_t \xi_{i,j} &= \partial_t \Xi_{i,j} = -\partial_t |\vec{x}_j - \vec{x}_i| = -(\vec{v}_j - \vec{v}_i) \cdot \vec{e}_{i,j}^{\,\text{n}} \\ \partial_t \zeta_{i,j} &= d_{i,j} \partial_t \Delta\psi_{i,j} = d_{i,j}\Big(\omega_i - \frac{(\vec{v}_j - \vec{v}_i) \cdot \vec{e}_{i,j}^{\,\text{t}}}{|\vec{x}_j - \vec{x}_i|}\Big) \end{aligned} \tag{34}$$

respectively.

3.4.2 Weak Links

For normal forces in weak links, we apply the Kelvin–Voigt model (KV) introduced in equation 2. In this context stress and strain are replaced by force and displacement, entailing the force

$$F_{i,j}^{\text{KV}} = -(k^{\,\text{n}} \xi_{i,j} + \gamma^{\,\text{n}} \partial_t \xi_{i,j}), \tag{35}$$

where $k^{\,\text{n}}$ is a calibration parameter[17] measured in kg/s^2 and $\gamma^{\,\text{n}}$ is a calibration parameter measured in kg/s. While this model is always defined and works for both attraction and repulsion, we only want the repulsive part to be in effect, so we truncate it to obtain the normal force

$$F_{i,j}^{\text{n}} = \min\{0, F_{i,j}^{\text{KV}}\}. \tag{36}$$

[16] The contact point assumption is discussed in appendix section D.

[17] Calibration parameters are discussed in greater detail in section 4.3.

To help fix the calibration parameters, we use the Brilliantov–Spahn–Hertzsch–Pöschel model (BSHP) alongside KV. It is a model for viscoelastic spheres and states [74] that the repulsive force

$$F_{i,j}^{\mathrm{BSHP}} = -\frac{2G\sqrt{2}}{3\nu}\Big(\frac{\nu}{1-\nu}\Big)\sqrt{\frac{2}{1/r_i + 1/r_j}}\big(\xi_{i,j}\sqrt{\xi_{i,j}} + \Lambda\sqrt{\xi_{i,j}}\partial_t\xi_{i,j}\big), \tag{37}$$

where [82] the dissipative constant

$$\Lambda = \frac{1}{3M}\Big(\frac{1-\nu}{\nu}\Big)^2\frac{(3\eta_K - \eta_G)^2}{3\eta_K + 2\eta_G}, \tag{38}$$

the shear and P-wave moduli are

$$G = \frac{Y}{2(1+\nu)} \qquad\qquad M = \frac{Y(1-\nu)}{(1-2\nu)(1+\nu)} \tag{39}$$

respectively, ν is the Poisson's ratio of the material and η_K is its bulk viscosity. This model is only defined for positive normal displacements and does not work correctly for attraction, so we must truncate it further than KV to obtain the normal force

$$F_{i,j}^{\mathrm{n}} = \begin{cases} \min\{0, F_{i,j}^{\mathrm{BSHP}}\}, & \xi_{i,j} \geq 0 \\ 0, & \xi_{i,j} \leq 0. \end{cases} \tag{40}$$

For tangential forces in weak links, we have two models. The first one is the Haff–Werner model (HW), which gives rise to dynamic friction [62] via the force

$$F_{i,j}^{\mathrm{HW}} = -\operatorname{sgn}(\partial_t\zeta_{i,j} + \partial_t\zeta_{j,i})\min\{\mu|F_{i,j}^{\mathrm{n}}|, \gamma^{\mathrm{t}}|\partial_t\zeta_{i,j} + \partial_t\zeta_{j,i}|\}, \tag{41}$$

where μ is the coefficient of friction from equation 1 and γ^{t} is a calibration parameter measured in kg/s. The second one is the Cundall–Strack model (CS), which features both static and dynamic friction in[18] the force

$$F_{i,j}^{\mathrm{CS}} = -\begin{cases} \operatorname{sgn}(\partial_t\zeta_{i,j} + \partial_t\zeta_{j,i})\mu|F_{i,j}^{\mathrm{n}}|, & \mu|F_{i,j}^{\mathrm{n}}| \leq k^{\mathrm{t}}|\zeta_{i,j} + \zeta_{j,i}| \\ \operatorname{sgn}(\zeta_{i,j} + \zeta_{j,i})k^{\mathrm{t}}|\zeta_{i,j} + \zeta_{j,i}|, & \mu|F_{i,j}^{\mathrm{n}}| > k^{\mathrm{t}}|\zeta_{i,j} + \zeta_{j,i}|, \end{cases} \tag{42}$$

where k^{t} is a calibration parameter measured in kg/s^2. These models allow us to choose between $F_{i,j}^{\mathrm{t}} = 0$ for no friction, $F_{i,j}^{\mathrm{t}} = F_{i,j}^{\mathrm{HW}}$ for dynamic friction and $F_{i,j}^{\mathrm{t}} = F_{i,j}^{\mathrm{CS}}$ for static and dynamic friction.

[18] There are conflicting accounts in literature [29, 62, 83] on what should determine the direction of the force, so our choice may look unfamiliar.

3.4.3 Strong Links

Similar to weak links, we use KV for normal forces in strong links too. The only difference is that we replace the normal displacement with the adjusted normal displacement to get

$$F_{i,j}^{\mathrm{aKV}} = -(\bar{k}^{\,\mathrm{n}}\Xi_{i,j} + \bar{\gamma}^{\,\mathrm{n}}\partial_t\Xi_{i,j}), \tag{43}$$

where $\bar{k}^{\,\mathrm{n}}$ is a calibration parameter measured in kg/s^2 and $\bar{\gamma}^{\,\mathrm{n}}$ is a calibration parameter measured in kg/s. Since strong links are both attractive and repulsive, we do not need to apply any truncations to obtain the normal force $F_{i,j}^{\mathrm{n}} = F_{i,j}^{\mathrm{aKV}}$.

For tangential forces in strong links, we simplify the Euler–Bernoulli model (EB) for beams [76] to create an angular analog of KV. This results in[19] the force

$$F_{i,j}^{\mathrm{EB}} = -(\bar{k}^{\,\mathrm{t}}\zeta_{i,j} + \bar{\gamma}^{\,\mathrm{t}}\partial_t\zeta_{i,j}), \tag{44}$$

where $\bar{k}^{\,\mathrm{t}}$ is a calibration parameter measured in kg/s^2 and $\bar{\gamma}^{\,\mathrm{t}}$ is a calibration parameter measured in kg/s. We cannot apply this model directly to the particles, however. To make it behave like a beam, we have to take both of its ends into account, so instead of following equations 6 and 7, the tangential force and torque have to be

$$F_{i,j}^{\mathrm{t}} = \frac{\tau_{i,j} + \tau_{j,i}}{|\vec{x}_j - \vec{x}_i|} \qquad\qquad \tau_{i,j} = r_i F_{i,j}^{\mathrm{EB}} \tag{45}$$

respectively. The benefit of this and other beam models is that they greatly reduce the number of particles needed for achieving high shear strength. For a chain of linked particles, the difference is similar to that of cooked and uncooked strands of pasta.

3.5 Breaking and Bonding

Since brittle materials behave elastically all the way up to their ultimate strengths, we can ignore plastic deformation and model fracture simply by breaking links once their yield strengths are reached. This is convenient, because it makes characterizing the material only require a few parameters and, just like with force models, there is a plethora of yield criteria [77] to choose from.

[19] We purposefully use the tangential displacement $\zeta_{i,j}$ instead of the angular displacement $\Delta\psi_{i,j}$ to make the beam favor bending near its thinner end, where it is also more likely to break.

In addition to breaking, some materials may do the opposite. For example fragments of ice may freeze together in the presence of water and crustal rocks may close cracks at very high pressures. Since this cannot happen in our system, we leave the spontaneous creation[20] of links out of our model.

3.5.1 Yield Criteria

For breaking strong links, we use the Zhang–Eckert criterion (ZE). It is intended for brittle materials and predicts fracture [77] when

$$\left(\frac{\sigma_{i,j}^{\mathrm{n}}}{\sigma^{\mathrm{crit\,n}}}\right)^2 + \left(\frac{\sigma_{i,j}^{\mathrm{t}}}{\sigma^{\mathrm{crit\,t}}}\right)^2 \geq 1, \tag{46}$$

where $\sigma_{i,j}^{\mathrm{n}}$ is the normal stress, $\sigma_{i,j}^{\mathrm{t}}$ is the tangential stress, $\sigma^{\mathrm{crit\,n}}$ is the ultimate normal strength and $\sigma^{\mathrm{crit\,t}}$ is the ultimate tangential strength. If the equation is interpreted as an elliptical disc in the stress space, the ratio of its semi-minor and semi-major axes

$$\beta = \frac{\sigma^{\mathrm{crit\,t}}}{\sigma^{\mathrm{crit\,n}}} \tag{47}$$

indirectly determines the fracture angle of the material. In terms of forces the criterion is

$$\left(\frac{F_{i,j}^{\mathrm{n}}}{\sigma^{\mathrm{crit\,n}}}\right)^2 + \left(\frac{F_{i,j}^{\mathrm{t}}}{\sigma^{\mathrm{crit\,t}}}\right)^2 \geq \left(\frac{(2\pi)}{2}(r_{i,j}^{\mathrm{crit}})^2\right)^2, \tag{48}$$

where the radius of the weakest point

$$r_{i,j}^{\mathrm{crit}} = \min\{r_i, r_j\} = r_{j,i}^{\mathrm{crit}}. \tag{49}$$

3.5.2 Random Variation

The ultimate strengths of real materials always exhibit some random variation. Statistically the strengths of random samples follow the three-parameter Weibull distribution [84], although not necessarily based on material constants [85].

Since our system is held together by strong links between differently sized particles, we cannot directly impose the Weibull distribution on their strengths and pretend that their geometries do not matter. As seen in equation 48, link strength is directly

[20] We still bring up bonding, because its contribution to the energy balance shows up in section 3.8.1.

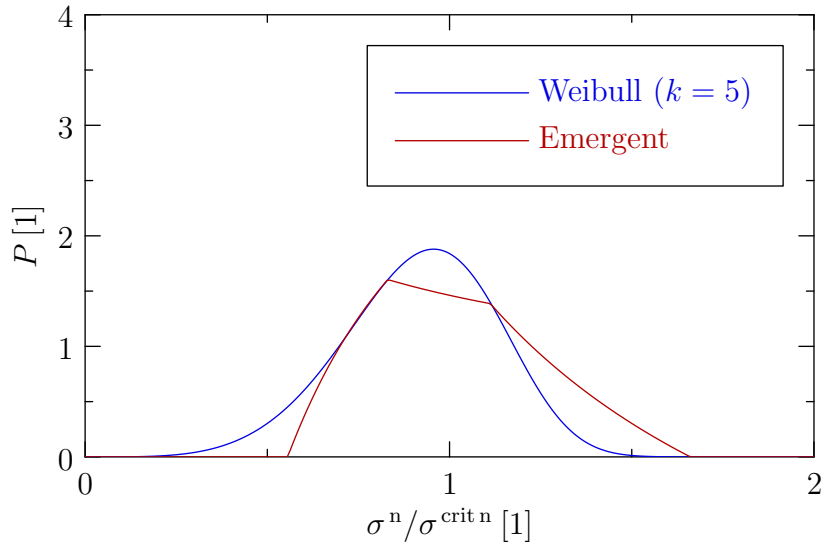

Figure 8: Comparing the emergent link strength distribution with the expected three-parameter Weibull distribution. The shape of the emergent distribution can be adjusted to match the Weibull modulus of the material as demonstrated.

proportional to the square of the radius of its weakest point, so we have to define the link strength factor s such that the modified yield criterion

$$\left(\frac{F^{\mathrm{n}}_{i,j}}{\sigma^{\mathrm{crit\,n}}}\right)^2 + \left(\frac{F^{\mathrm{t}}_{i,j}}{\sigma^{\mathrm{crit\,t}}}\right)^2 \geq \left(\frac{(2\pi)}{2}(s_{i,j}r^{\mathrm{crit}}_{i,j})^2\right)^2 \tag{50}$$

faithfully reproduces the desired strength distribution.

We assume that s and r are independently and uniformly distributed, because doing so makes all of the resulting random quantities bounded and allows us to calculate a closed form[21] for the emergent strength distribution. The emergent distribution does not match the expected Weibull distribution exactly, but it is a decent approximation as seen in figure 8.

While the figure shows the case for the Weibull modulus $k = 5$, we could reach any other k by adjusting the bounds of s and r. The only problem is that going too far into $k > 5$ would require making the distribution of r so narrow that it negatively affects the disorder[22] of the system. Avoiding this problem without giving up the previously mentioned nice properties would require making s and r correlated in some manner.

[21] The emergent distribution is calculated in appendix section E.

[22] The importance of disorder is discussed in section 3.7.2.

3.6 Time Development

Disregarding models[23] with quantized time, there are two primary ways to advance time. Force-based time development involves advancing time by a small step, moving the particles accordingly, checking for collisions and repeating the process until enough time has passed. Event-driven time development, on the other hand, involves calculating the trajectories of the particles to predict when the next collision is going to happen, advancing time to that moment, resolving the collision and repeating the process until enough time has passed.

Consequently, event-driven time development works better for sparse systems with infrequently colliding particles, whereas force-based time development is more suitable for dense systems with persistent contacts. Our system falls into the latter category, which is why we opt for force-based time development.

3.6.1 Equations of Motion

Once the forces and torques are known, classical mechanics dictates the subsequent behavior of the system. Assuming that the density of the particles ρ is constant, each particle i gets the linear and angular accelerations

$$\vec{a}_i = \frac{\vec{F}_i}{m_i} \qquad\qquad \alpha_i = \frac{\tau_i}{J_i} \tag{51}$$

respectively, where the mass

$$m_i = \frac{2\,(2\pi)}{3}\rho r_i^3 \tag{52}$$

and the moment of inertia

$$J_i = \frac{2}{5}m_i r_i^3 = \frac{4\,(2\pi)}{15}\rho r_i^5. \tag{53}$$

Following these definitions, other dynamical quantities develop according to

$$\begin{aligned} \vec{v}_i &= \int_0^t \mathrm{d}t\,\vec{a}_i & \omega_i &= \int_0^t \mathrm{d}t\,\alpha_i \\ \vec{x}_i &= \int_0^t \mathrm{d}t\,\vec{v}_i & \varphi_i &= \int_0^t \mathrm{d}t\,\omega_i. \end{aligned} \tag{54}$$

We only need some way to evaluate the integrals.

[23] Cellular automata are sometimes used for simulating granular systems [86] and feature quantized time.

3.6.2 Integration Methods

There are many methods for iteratively calculating the integrals that appear in the equations of motion [87]. They all produce the same result as the time step Δt is brought to zero, but at a different computational cost. It is therefore important to choose the appropriate combination of integration method and time step to maximize efficiency.

The simplest option is the forward Euler method, stating[24] that

$$\begin{aligned} \vec{v}(t+\Delta t) &= \vec{v}(t) + \vec{a}(t)\Delta t \\ \vec{x}(t+\Delta t) &= \vec{x}(t) + \vec{v}(t)\Delta t. \end{aligned} \tag{55}$$

The Euler method is not particularly accurate, but may be gradually improved through higher-order Taylor expansions. For example second-order expansions lead to

$$\begin{aligned} \vec{v}(t+\Delta t) &= \vec{v}(t) + \vec{a}(t)\Delta t \\ \vec{x}(t+\Delta t) &= \vec{x}(t) + \vec{v}(t)\Delta t + \frac{1}{2}\vec{a}(t)(\Delta t)^2. \end{aligned} \tag{56}$$

Even more accuracy can be obtained with predictor–corrector methods, such as the modified Beeman's or Kuraev's algorithm for damped systems [88]. The former involves initially making a prediction with

$$\begin{aligned} \vec{v}^{\,\mathrm{pred}}(t+\Delta t) &= \vec{v}(t) + \Big(\frac{3\vec{a}(t) - \vec{a}(t-\Delta t)}{2}\Big)\Delta t \\ \vec{x}^{\,\mathrm{pred}}(t+\Delta t) &= \vec{x}(t) + \vec{v}(t)\Delta t + \frac{1}{2}\Big(\frac{4\vec{a}(t) - \vec{a}(t-\Delta t)}{3}\Big)(\Delta t)^2, \end{aligned} \tag{57}$$

then using the prediction to calculate $\vec{a}(t+\Delta t)$ and finally replacing the prediction with the correction

$$\begin{aligned} \vec{v}^{\,\mathrm{corr}}(t+\Delta t) &= \vec{v}(t) + \Big(\frac{2\vec{a}(t+\Delta t) + 5\vec{a}(t) - \vec{a}(t-\Delta t)}{6}\Big)\Delta t \\ \vec{x}^{\,\mathrm{corr}}(t+\Delta t) &= \vec{x}(t) + \vec{v}(t)\Delta t + \frac{1}{2}\Big(\frac{\vec{a}(t+\Delta t) + 2\vec{a}(t)}{3}\Big)(\Delta t)^2. \end{aligned} \tag{58}$$

While these and other higher-order methods provide improved accuracy, they also tend to be less stable. Since it is much more important for us to maintain contacts than to calculate trajectories, the Euler method beats the other methods simply by the virtue of making it more affordable to decrease the time step.

[24] In this context angular quantities work exactly the same as their linear counterparts, so we do not write them out explicitly. The reader may replace $\vec{x}$ with φ, $\vec{v}$ with ω, $\vec{a}$ with α and m with J at their leisure.

3.6.3 Time Step

The time step can be chosen with a certain arbitrariness, although there are upper bounds for ensuring the correct reproduction of various phenomena. Technically, there is also a lower bound imposed by the precision of the underlying number representation, but it can always be eliminated by choosing the units of time carefully.

The most important upper bound is the one for numerical stability, because violating it will make the integration error grow exponentially, which manifests as the system exploding violently. Another essential upper bound is the point at which energy is almost completely conserved. The time step at which these bounds are satisfied is collectively known as the critical time step and it is strongly influenced by both the integration method and the dynamics of the system. The least upper bound is usually impossible to determine, but guidelines exist for getting close to it. To give some examples, a densely packed system integrated with the central difference method [89] should satisfy $f\Delta t < 1/21$, where f is the characteristic frequency of oscillations, and another such system integrated with the third-order Gear method [90] should satisfy $\Delta t/T < 1/50$, where T is the characteristic duration of collisions.

In addition to energy conservation, there is the question of waves. The speeds of primary and secondary elastic waves in a solid are

$$c^{\mathrm{P}} = \sqrt{\frac{K + 4G/3}{\rho}} \qquad\qquad c^{\mathrm{S}} = \sqrt{\frac{G}{\rho}} \tag{59}$$

respectively, where the bulk modulus

$$K = \frac{Y}{3(1 - 2\nu)}. \tag{60}$$

If accurate modeling of wave propagation is desired, the time step should be such that

$$\frac{c^{\mathrm{P}}\Delta t}{2R} < 1, \tag{61}$$

where R is the characteristic radius of the particles.

Intuitively it would make sense for cracks to obey the same speed limit as waves, but this is not always the case. Cracks may propagate an order of magnitude faster than elastic waves [91, 92], which requires adjusting the time step constraint to

$$\frac{c^{\mathrm{P}}\Delta t}{2R} < \frac{1}{\mathrm{Ma}}, \tag{62}$$

where Ma is the characteristic Mach number of the cracks.

3.7 Initial and Boundary Conditions

Before starting the shearing process, we must create the block of material and break it into two halves. We also need some way to ensure that the lower half stays in place when the upper half is moved. These issues are best addressed with periodic boundaries and a packing process that features automatic quality assurance.

3.7.1 Periodic Boundaries

Ideally the two halves of the block would always be on top of each other, but that would require making them infinitely long in the direction of the shearing. Simulating an infinite system like that is obviously impossible, but we can still imitate the infinity through periodic boundary conditions. Mathematically this involves replacing the usual metric of our space

$$d_{i,j} = \sqrt{(x_j^{\mathrm{x}} - x_i^{\mathrm{x}})^2 + (x_j^{\mathrm{y}} - x_i^{\mathrm{y}})^2} \tag{63}$$

with the horizontal minimum image metric

$$d_{i,j} = \sqrt{\left((x_j^{\mathrm{x}} - x_i^{\mathrm{x}}) - l^{\mathrm{x}} \left\lfloor \frac{x_j^{\mathrm{x}} - x_i^{\mathrm{x}}}{l^{\mathrm{x}}} + \frac{1}{2} \right\rfloor\right)^2 + (x_j^{\mathrm{y}} - x_i^{\mathrm{y}})^2}. \tag{64}$$

This effectively tiles the space with infinitely many copies of one of its regions. It introduces some nonphysical effects as well, but we can make them arbitrarily small by increasing the length of the region.

3.7.2 Particle Size Distribution

If we made the block from particles that all have the same size, the system would quickly transition into an anisotropic state. We can avoid this problem by making the sizes of the particles random, but there is still the question of choosing the right particle size distribution.

A similar phenomenon arises in colloidal suspensions, where a system of spherical particles spontaneously transitions from a disordered state into an ordered one. Theoretical and experimental results suggest [65] that if the particle sizes[25] are normally distributed with the mean μ and the standard deviation σ, the transition happens roughly when

$$\frac{\sigma}{\mu} < 0.1. \tag{65}$$

[25] In this context, unlike in chemistry, particle size is defined by radius instead of by mass.

It turns out that we can adapt this result to a uniform particle size distribution and barely avoid the transition by choosing the endpoints of the interval[26] according to

$$r^{\min} = \left(\frac{2}{1+\sqrt{2}}\right) r^{\text{avg}} \qquad\qquad r^{\max} = \left(\frac{4}{2+\sqrt{2}}\right) r^{\text{avg}}, \tag{66}$$

where r^{avg} is the average particle size. A wider interval would also work, but not without making it harder to adjust[27] the Weibull modulus of the material.

3.7.3 Particle Packing

Once the geometry of the particles is known, we take the following steps to pack them together. The process may not be optimal, but it is very flexible and produces a dense packing without introducing any new machinery.

First, we generate an excessive number of particles and arrange them into a square lattice. We make the lattice loose enough to allow every particle to be displaced by Δx in any direction without coming into contact with another particle. Second, we randomly perturb each particle by a displacement smaller than or equal to Δx. This is not strictly necessary, but makes the rest of the steps go faster. Third, we disable static friction and enable the harmonic potential

$$U_i = \frac{1}{2} k^{\text{ext}} \left(x_i^{\text{y}} - \frac{l^{\text{y}}}{2}\right)^2, \tag{67}$$

where k^{ext} is a calibration parameter measured in kg/s^2. We may also increase the viscosity of the surrounding media to make the potential energy dissipate faster. Fourth, we wait until the particles settle into a stable configuration, remove the excess particles and restore the original force models. The potential is defined such that the pressure at the end should be consistent throughout the block.

3.7.4 Quality Assurance

When we perform the packing, we want the result to be as dense as possible while remaining disordered. Such a result is commonly known as a random close packing (RCP) or, following a more precise definition [93], a maximally random jammed state (MRJ). Since density and disorder are necessarily at odds with each other, it is difficult to tell whether any given packing is sufficiently dense or disordered. We

[26] The equations for the endpoints of the interval are derived in appendix section F.

[27] The effects of the random variation are discussed in section 3.5.2.

can visually inspect the packing to see if it looks acceptable, but this is laborious and susceptible to a biased judgment. It is therefore desirable to employ some quantitative metrics to assess the quality of the packing.

Density is easy to quantify by calculating the packing fraction

$$q = \frac{(2\pi)}{2}\left(\frac{N}{l^{\mathrm{x}} l^{\mathrm{y}}}\right)\frac{1}{N}\sum_i r_i^2, \tag{68}$$

which should always be[28] between 0 and $(2\pi)/6\sqrt{2}$. For identical hard spheres in MRJ, typical packing fractions vary from $q \approx 0.60$ [94] to $q \approx 0.68$ [95] due to differences in the packing process. To account for this variation, we only require that the packing fraction is reasonable and adjust the density of the particles ρ based on the true material density.

Disorder is a bit harder to quantify. There exist order metrics like the orientational Q metric or the translational T metric [93], but they only work with respect to an ordered reference structure. It is more appropriate for us to use the two-body excess entropy [96], which has the dimensionless form

$$\frac{S}{k^{\mathrm{B}}} = -\frac{1}{2}\left(\frac{N}{l^{\mathrm{x}} l^{\mathrm{y}}}\right)\int_0^\infty \mathrm{d}d\,\Big(g\log g - (g-1)\Big), \tag{69}$$

where g is the radial distribution function parametrized by the distance d and k^{B} is the Boltzmann constant. It is similar to thermodynamic entropy in that it grows with increasing disorder and only its differences admit meaningful interpretations.

3.7.5 Block Formation

To turn a packing into a block of material, we establish a maximum distance for qualifying as a nearest neighbor and bond each particle with its neighbors by adding strong links between them. If the packing is not ideal or the force models for weak and strong links differ at this point, the bonding will introduce stresses inside the material. This problem can be alleviated by giving the system enough time to reach a stable configuration again, but doing so does not completely eliminate all of the stresses.

[28] The packing fraction is discussed in appendix section B.

3.7.6 Fault Creation

After forming the block, we split it into two halves by partitioning the particles into two groups with an indicator function and breaking all the strong links that span both groups. To give some examples of the indicator function δ, a straight fault can be created by grouping each particle i according to

$$\delta_i = \begin{cases} 0, & x_i^{\mathrm{y}} < l^{\mathrm{y}}/2 \\ 1, & x_i^{\mathrm{y}} \geq l^{\mathrm{y}}/2 \end{cases} \tag{70}$$

while a jagged fault can be created with

$$\delta_i = \begin{cases} 0, & x_i^{\mathrm{y}} < l^{\mathrm{y}}/2 + (h/2)\sin(_{(2\pi)}\, n x_i^{\mathrm{x}}/l^{\mathrm{x}}) \\ 1, & x_i^{\mathrm{y}} \geq l^{\mathrm{y}}/2 + (h/2)\sin(_{(2\pi)}\, n x_i^{\mathrm{x}}/l^{\mathrm{x}}), \end{cases} \tag{71}$$

where h is the height and n is the number of jags.

3.8 Estimators

Making measurements in an experiment can be very difficult, because it requires the careful selection, placement and reading of sensors. Fortunately, simulations make the same task comparatively trivial. Since the state of the system is always known in its entirety, we either can read our measurements directly from the data structures or calculate them with the appropriate estimators. The only limitations stem from the computational feasibility of the estimators we devise.

3.8.1 Energy

Conservation of energy mandates that the total energy of the system matches the work done on it, as in

$$E^{\,\mathrm{kin}} + E^{\,\mathrm{cont}} + E^{\,\mathrm{ext}} + Q^{\,\mathrm{amb}} + Q^{\,\mathrm{fric}} + Q^{\,\mathrm{brk}} = W^{\,\mathrm{bond}} + W^{\,\mathrm{driv}}, \tag{72}$$

where $E^{\,\mathrm{kin}}$ is the kinetic energy, $E^{\,\mathrm{cont}}$ is the stored contact energy, $E^{\,\mathrm{ext}}$ is the external potential energy, $Q^{\,\mathrm{amb}}$ is the energy dissipated by ambient forces, $Q^{\,\mathrm{fric}}$ is the energy dissipated by contact friction, $Q^{\,\mathrm{brk}}$ is the energy lost in removing contacts, $W^{\,\mathrm{bond}}$ is the energy expended to create contacts and $W^{\,\mathrm{driv}}$ is the work done by the driving force.

Even though heat is not the only energy dissipation mechanism in play, we use its symbol Q to distinguish the dissipative quantities from the rest. This distinction is of practical importance, because conservative quantities are completely determined by the current state of the system, whereas dissipative quantities require evaluating line integrals over the entire history of the system.

The energies consist of the individual contributions of the particles and their links, that is,

$$\begin{aligned} E^{\,\mathrm{kin}} &= \sum_i E_i^{\mathrm{kin}} & Q^{\,\mathrm{amb}} &= \sum_i Q_i^{\mathrm{amb}} \\ E^{\,\mathrm{cont}} &= \sum_i \sum_j^{j>i} E_{i,j}^{\mathrm{cont}} & Q^{\,\mathrm{fric}} &= \sum_i \sum_j^{j>i} Q_{i,j}^{\mathrm{fric}} \\ E^{\,\mathrm{ext}} &= \sum_i U_i & Q^{\,\mathrm{brk}} &= \sum_i Q_i^{\mathrm{brk}} \\ W^{\,\mathrm{bond}} &= \sum_i W_i^{\mathrm{bond}} & W^{\,\mathrm{driv}} &= \sum_i W_i^{\mathrm{driv}}. \end{aligned} \tag{73}$$

The kinetic terms are always

$$E_i^{\mathrm{kin}} = \frac{1}{2}(m_i|v_i|^2 + J_i\omega_i^2) \qquad Q_i^{\mathrm{amb}} = \Big|\int_0^t \mathrm{d}t(\vec{v}_i \cdot \vec{F}_i^{\,\mathrm{amb}} + \omega_i \tau_i^{\,\mathrm{amb}})\Big|. \tag{74}$$

The contact terms $E_{i,j}^{\mathrm{cont}}$ and $Q_{i,j}^{\mathrm{fric}}$ depend on the conservative and dissipative parts of the force models respectively. The conservative parts are

$$\begin{aligned} E_{i,j}^{\mathrm{cont\,KV}} &= \frac{1}{2}k^{\,\mathrm{n}}\xi_{i,j}^2 \\ E_{i,j}^{\mathrm{cont\,BSHP}} &= \frac{4G\sqrt{2}}{15\nu}\Big(\frac{\nu}{1-\nu}\Big)\sqrt{\frac{2}{1/r_i + 1/r_j}}\Big(\xi_{i,j}^2\sqrt{\xi_{i,j}}\Big) \end{aligned} \tag{75}$$

and either

$$E_{i,j}^{\mathrm{cont\,HW}} = 0 \qquad E_{i,j}^{\mathrm{cont\,CS}} = \frac{1}{2}k^{\,\mathrm{t}}\zeta_{i,j}^2 \tag{76}$$

for weak links and

$$E_{i,j}^{\mathrm{cont\,aKV}} = \frac{1}{2}k^{\,\mathrm{n}}\Xi_{i,j}^2 \qquad E_{i,j}^{\mathrm{cont\,EB}} = \frac{1}{2}\bar{k}^{\,\mathrm{t}}(\zeta_{i,j}^2 + \zeta_{j,i}^2) \tag{77}$$

for strong links. The dissipative parts are their complements, so the expression for the whole term[29] is

$$Q_{i,j}^{\mathrm{fric}} = \Big|\int_{t_{i,j}^{\mathrm{init}}}^t \mathrm{d}t(F_{i,j}^{\mathrm{n}}\partial_t\xi_{i,j} + F_{i,j}^{\mathrm{t}}\partial_t\zeta_{i,j})\Big| - E_{i,j}^{\mathrm{cont}}. \tag{78}$$

[29] Actually, $t_{i,j}^{\mathrm{init}}$ may not always exist or be unique, but we pretend that it is to keep the expression short.

The term for the driving force is just

$$W_i^{\text{driv}} = \Big| \int_0^t \mathrm{d}t\, \vec{v}_i \cdot \vec{F}_i^{\text{driv}} \Big| \tag{79}$$

and the breaking and bonding terms $Q_{i,j}^{\text{brk}}$ and $W_{i,j}^{\text{bond}}$ are the same as $E_{i,j}^{\text{cont}}$, but occur instantaneously when adding or removing links.

3.8.2 Entropy

As seen in equation 69, calculating the two-body excess entropy requires integrating over the radial distribution function, which in turn requires integrating over the whole space. For a finite number of particles, this involves gathering all their pairwise distances into a weighted sample, formulating an estimate of the true population based on the sample, constructing the radial distribution function from the estimate and evaluating the resulting integral.

We define the samples and their weights as

$$d_{i,j} = |\vec{x}_j - \vec{x}_i| \qquad\qquad w_{i,j} = \frac{A_{i,j}^{\bigcirc}}{A_{i,j}^{\otimes}}, \tag{80}$$

where $A_{i,j}^{\bigcirc}$ is the surface area of a spherical shell with the radius $d_{i,j}$ and $A_{i,j}^{\otimes}$ is the surface area of the same shell when positioned at $\vec{x}_i$ and truncated[30] within the block of material. Using weighted kernel density estimation, we take the population probability density to be

$$P = \frac{Z}{B}\Big(\sum_i \sum_j^{j\neq i} w_{i,j}\Big)^{-1} \sum_i \sum_j^{j\neq i} w_{i,j} \Psi\Big(\frac{d - d_{i,j}}{B}\Big), \tag{81}$$

where Ψ is a statistical kernel, B is its bandwidth and Z is a normalization constant for enforcing

$$\int_0^{l^{\mathrm{x}}/4} \mathrm{d}d\, P = 1. \tag{82}$$

The radial distribution function is now easily stated as

$$g = \frac{V^{\bigcirc}}{A^{\bigcirc}} P = \frac{(l^{\mathrm{x}}/4)^2}{2d} P, \tag{83}$$

[30] Finding the surface area of the truncated part becomes deceivingly complicated as the number of dimensions is increased [97].

where $V^{\bigcirc}$ is the volume of a sphere with the radius $l^{\mathrm{x}}/4$ and $A^{\bigcirc}$ is the surface area of a spherical shell with the radius d. We may also simplify the expression for the entropy to

$$\frac{S}{k^{\mathrm{B}}} = -\frac{1}{2}\Big(\frac{N}{l^{\mathrm{x}} l^{\mathrm{y}}}\Big)\Big(\frac{l^{\mathrm{x}}}{4} + \int_0^{l^{\mathrm{x}}/4} \mathrm{d}d\, g(\log g - 1)\Big). \tag{84}$$

Theoretically the integrals would require taking the limit as the distance goes to infinity, but we have to limit ourselves to $l^{\mathrm{x}}/4$, because otherwise the periodic boundaries of the system[31] would create false correlations. This limitation also has the unfortunate side effect of introducing Z into equation 81 to keep P normalized.

3.8.3 Dry Friction

In comparison to energy and entropy, estimating the coefficient of friction is delightfully simple. Using equation 1, we can calculate it directly from the load with

$$\mu = \frac{1}{N^{\,\mathrm{driv}}} \sum_i \frac{F_i^{\mathrm{driv\,x}}}{F_i^{\mathrm{driv\,y}}} \tag{85}$$

or indirectly from the force feedback with

$$\mu = \frac{1}{N^{\,\mathrm{driv}}} \sum_i \frac{F_i^{\mathrm{x}} - F_i^{\mathrm{driv\,x}}}{F_i^{\mathrm{y}} - F_i^{\mathrm{driv\,y}}}. \tag{86}$$

These estimators produce the same value when the motion is steady, but consistently differ otherwise. Both of them are useful, because their difference provides some insight into the dynamics of the system.

[31] The periodic boundaries are discussed in section 3.7.1.

4 Practical Implementation

The goal of this section is to highlight the most interesting points that came up in the practical implementation of the simulation. While these points are most relevant to our own program [98], they should also shed some light on the challenges faced by other DEM projects [99–101].

4.1 Properties of Granite

Granite is not a single unambiguous material, but covers a wide range of coarse-grained rocks primarily consisting of quartz and feldspar. Figure 9 shows what a typical slab of granite looks like, although it should be noted that the colors and grain sizes of different granites vary greatly.

As granites are so varied, they do not have a complete and consistent naming convention. Instead, they are commonly named after their origins or most prominent secondary constituents. The samples in figure 4 are of Barre[32] granite and the slab in figure 9 is of Kure[33] granite, for example. Since our primary goal is not the accurate representation of any particular granite, we mix and match the properties of several different granites to obtain a fictitious but believable compromise.

Our granite shall have the density $\rho = (2.7 \pm 0.1) \cdot 10^3\,\mathrm{kg/m^3}$ [102], the Young's modulus $Y = (50 \pm 20)\,\mathrm{GPa}$ [103] and the Poisson's ratio $\nu = 0.22 \pm 0.12$ [104]. Since our system is always under a compressive load, the ultimate normal strength of links shall be $\sigma^{\mathrm{crit\,n}} = (280 \pm 30)\,\mathrm{MPa}$ [70], and since the load is rarely much larger than the ultimate strength, the coefficient of friction between particles shall be $\mu = 0.7 \pm 0.1$ [69]. The ultimate tangential strength follows from the axial ratio in equation 47, which we assume to be $\beta = 0.6 \pm 0.1$ [77]. We also assume that the Weibull modulus $k = 5$, which is on the lower end of the expected $k = 15 \pm 10$ [84] due to the small scale of our particles.

In our system the block of granite is immersed in air, which is a fluid with the

[32] The origin is Barre, Vermont, USA.
[33] The origin is Kure, Hiroshima, Japan.

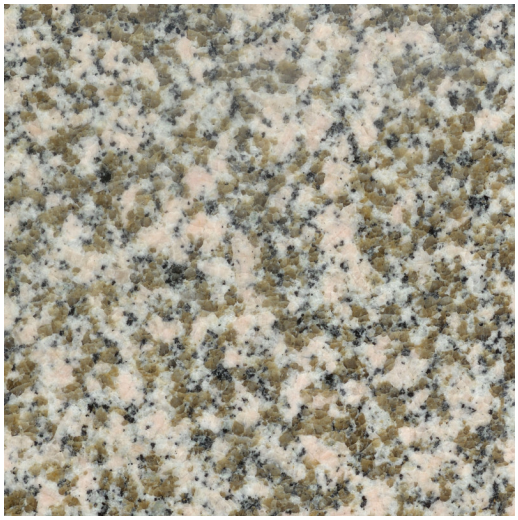

(a) View of a 100 mm region.

(b) Close-up view with the magnification $X = 4$.

Figure 9: Typical surface texture of a polished slab of granite.

dynamic viscosity $\eta_G^{\text{amb}} = (18 \pm 3)\,\mu\text{Pa s}$ [105]. This makes the ambient forces and torques predicted by equations 18 and 19 negligibly small, so we might as well set $\vec{F}_i^{\,\text{amb}} = 0$ and $\tau_i^{\text{amb}} = 0$.

4.2 Simulation Parameters

There are a few things in the simulation that are not tied to material properties or other physical restrictions. We can choose them with a certain degree of arbitrariness, although there are some choices that work better than others.

We make the average particle size $r^{\text{avg}} = 1\,\text{mm}$ to approximately match the visible grain size of granite. We want there to be a few thousand such particles, so we make the side lengths of our system $l^{\text{x}} = l^{\text{y}} = 100\,\text{mm}$. To overcome static friction without generating excessive amounts of heat, we set the horizontal target speed to $v^{\text{driv}} = 2\,\text{m/s}$ and vary the vertical target pressure over $0 < p^{\text{driv}}/\sigma^{\text{crit n}} \leq 1$. Since we want the total strain to eventually reach $\varepsilon = 1$, we set the total simulation time to $t^{\text{fin}} - t^{\text{init}} = 50\,\text{ms}$.

Based on the properties laid out in section 4.1, equation 59 predicts that the speeds of different kinds of elastic waves in our material are $c^{\text{P}} = (4.6 \pm 2.1)\,\text{km/s}$ and $c^{\text{S}} = (2.8 \pm 0.8)\,\text{km/s}$. Assuming that cracks always propagate at $\text{Ma} < 15$, equation 62 suggests that the time step should satisfy $\Delta t < 18\,\text{ns}$. By adding in a

safety factor of 1.5, we end up with $\Delta t = 10\,\mathrm{ns}$.

In order to reproduce the link strength distribution with the appropriate Weibull modulus, we limit the link strength factors to $0.9 < s_{i,j} < 1.1$. We also make the fault slightly jagged by using the indicator function in equation 71 with the parameters $n = 4$ and $h = 4\,\mathrm{mm}$. This does not make a noticeable difference in the measurements we are interested in, but helps decouple the initial fragmentation from the exact arrangement of the particles.

4.3 Calibration

Calibration typically involves a lot of trial and error, making it the most laborious part of the implementation. While there exist tables [78] and guidelines [63] for calibrating various models, the details always depend on the particular system and its desired properties. We only take the calibration far enough to make the comparison of models possible.

The calibration parameters we need to fix are k^{n} and γ^{n} in equation 35, k^{t} in equation 42, γ^{t} in equation 41, $\bar{k}^{\mathrm{n}}$ and $\bar{\gamma}^{\mathrm{n}}$ in equation 43, $\bar{k}^{\mathrm{t}}$ and $\bar{\gamma}^{\mathrm{t}}$ in equation 44 and k^{ext} in equation 67. The parameters affect the material such that k^{n}, $\bar{k}^{\mathrm{n}}$ and $\bar{k}^{\mathrm{t}}$ determine its elastic properties, γ^{n}, $\bar{\gamma}^{\mathrm{n}}$ and $\bar{\gamma}^{\mathrm{t}}$ mostly determine its viscous properties, k^{t} and γ^{t} influence its internal friction and k^{ext} slightly influences its fracture energy.

We introduced BSHP in section 3.4.2 with the intention to draw parallels between the calibration parameters of KV and other known properties of the material. Doing so helps us first fix k^{n} and γ^{n}, laying the foundations for the rest of the calibration parameters.

Let us begin by exploring a situation, where two strongly linked particles i and j with $r_i = r_j$ break apart just as $\partial_t \xi_{i,j} = 0$ and $F^{\mathrm{t}}_{i,j} = 0$. At that moment the yield criterion in equation 50 is barely satisfied, so

$$\left(\frac{F^{\mathrm{n}}_{i,j}}{\sigma^{\,\mathrm{crit\,n}}}\right)^2 = \left(\frac{(2\pi)}{2}(s_{i,j} r_i)^2\right)^2. \tag{87}$$

After the link is broken, equation 35 predicts that the force should be

$$F^{\mathrm{KV}}_{i,j} = -k^{\mathrm{n}} \xi_{i,j}, \tag{88}$$

making the normal displacement

$$\xi_{i,j} = \frac{r_i}{2}\left(\frac{r_i}{k^{\mathrm{n}}} s^2_{i,j}\,(2\pi)\,\sigma^{\,\mathrm{crit\,n}}\right), \tag{89}$$

while equation 37 predicts that the force should be

$$F_{i,j}^{\text{BSHP}} = -\frac{2G\sqrt{2}}{3\nu}\left(\frac{\nu}{1-\nu}\right)\sqrt{r_i}\left(\xi_{i,j}\sqrt{\xi_{i,j}}\right), \tag{90}$$

making the normal displacement

$$\xi_{i,j} = \frac{r_i}{2}\left(\frac{3\nu}{2G}\left(\frac{1-\nu}{\nu}\right)s_{i,j}^2\,(2\pi)\,\sigma^{\,\text{crit n}}\right)^{2/3}. \tag{91}$$

For the displacements to be consistent, we would need to have

$$k^{\,\text{n}} = r_i\left(\frac{2G}{3\nu}\left(\frac{\nu}{1-\nu}\right)s_{i,j}\sqrt{(2\pi)\,\sigma^{\,\text{crit n}}}\right)^{2/3} = (8\pm 7)\cdot 10^6\,\frac{\text{kg}}{\text{s}^2}, \tag{92}$$

so we choose $k^{\,\text{n}} = 10^7\,\text{kg/s}^2$ and run a few simulations to verify that it produces the appropriate stress–strain curves.

We can do a similar trick to fix $\gamma^{\,\text{n}}$, although we need to address another problem first. The dissipative constant Λ in equation 38 is very sensitive to changes in the dynamic and bulk viscosities η_G and η_K, both of which are very large and not known exactly [71]. Fortunately, there is another way to calculate Λ from the dynamics of particle impacts [82, 106]. Given two 1 m granite spheres colliding at $v = 1\,\text{m/s}$, their coefficient of restitution $\Upsilon = 0.83 \pm 0.06$ [107]. In this case, the dissipative constant has the first-order approximation

$$\Lambda = \frac{1-\Upsilon}{D(\rho^2 v)^{1/5}} = (6\pm 3)\cdot 10^{-3}\,\frac{1}{\text{s}}, \tag{93}$$

where $D = 1.15$.

We can now explore the same situation as before, but without imposing any constraints on $\xi_{i,j}$ or $\partial_t \xi_{i,j}$. Due to the linear independence of displacements and their rates of change, we can unify

$$F_{i,j}^{\text{KV}} = -\gamma^{\,\text{n}}\partial_t \xi_{i,j} \tag{94}$$

with

$$F_{i,j}^{\text{BSHP}} = -\frac{2G\sqrt{2}}{3\nu}\left(\frac{\nu}{1-\nu}\right)\sqrt{r_i}\left(\Lambda\sqrt{\xi_{i,j}}\partial_t \xi_{i,j}\right) \tag{95}$$

to obtain

$$\gamma^{\,\text{n}} = \frac{2G\sqrt{2}}{3\nu}\left(\frac{\nu}{1-\nu}\right)\sqrt{r_i}\left(\Lambda\sqrt{\xi_{i,j}}\right). \tag{96}$$

Since the resulting equation depends on $\xi_{i,j}$, we can only use it to derive the upper bound

$$\gamma^{\mathrm{n}} < \Lambda r_i \left(\frac{2G}{3\nu} \left(\frac{\nu}{1-\nu} \right) s_{i,j} \sqrt{(2\pi)\, \sigma^{\mathrm{crit\,n}}} \right)^{2/3} = (7 \pm 6) \cdot 10^4 \, \frac{\mathrm{kg}}{\mathrm{s}}. \tag{97}$$

Even though this bound has a very large uncertainty, it is useful for finding the right order of magnitude. After some searching, we settle on $\gamma^{\mathrm{n}} = 10^1 \, \mathrm{kg/s}$ and run a handful of simulations to ensure particle impacts behave as expected.

As alluded to in section 3.7.5, the forces in weak and strong links should agree when breaking or bonding happens, so it is reasonable to assume that $\bar{k}^{\mathrm{n}} = k^{\mathrm{n}}$ and $\bar{\gamma}^{\mathrm{n}} = \gamma^{\mathrm{n}}$. Another reasonable assumption is that the material should be equally stiff in normal and tangential directions, so we also assume that $\bar{k}^{\mathrm{t}} = \bar{k}^{\mathrm{n}}$ and $\bar{\gamma}^{\mathrm{t}} = \bar{\gamma}^{\mathrm{n}}$.

Once the material behaves as intended, we choose the frictional parameters k^{t} and γ^{t} such that the cases in equations 41 and 42 are balanced. This may not produce the most realistic result, but ensures that neither dynamic nor static friction absolutely dominate. We therefore assume that $k^{\mathrm{t}} = 10^8 \, \mathrm{kg/s^2}$ and $\gamma^{\mathrm{t}} = 10^2 \, \mathrm{kg/s}$ and verify that simulations of rolling and piling particles work as they should.

The remaining choice of k^{ext} does not matter much, so we decide that $k^{\mathrm{ext}} = 10^2 \, \mathrm{kg/s^2}$ and run some simulations to check that it does not skew the fracture energy.

4.4 Performance Considerations

There are countless ways to improve the performance of the implementation. Aside from more powerful hardware or better software engineering, choosing those algorithms with the lowest complexity classes for the tasks that work on the largest inputs makes the biggest difference. In terms of programming effort, identifying the longest independent computations and making them run in parallel can also be very effective.

4.4.1 Cell Lists

If done naively, calculating pair interactions would scale quadratically[34] with respect to the number of particles. However, by using an arrangement known as cell lists, we can make the calculations only scale quadratically with respect to the number of neighboring particles and linearly with respect to the total number of particles. The idea behind the algorithm is to divide the system into small disjoint cells, each of which maintains a list of all the particles it contains. The pair interactions are then calculated by only considering those particles that are in adjacent cells and less than some cutoff distance away from each other. Due to the symmetric nature of pair interactions, we only need to consider each interaction from the perspective of one of the particles, which allows us to further cut the computational burden into half.

To keep things simple, we employ rectangular cells with the side lengths l^{cell}, except for those cells that are on the edges and extend to infinity. As a consequence, we have to choose the cutoff distance d^{cut} such that

$$2r^{\max} < d^{\text{cut}} < \min l^{\text{cell}}. \tag{98}$$

Now, as illustrated in figure 10, a particle may only interact with another particle

- if it is contained in the same cell as the other particle and has a smaller index than the other particle or
- if it is contained in a cell that is adjacent to the cell that contains the other particle and its cell has a smaller index than the other cell.

While these rules may sound arbitrary and confusing, they admit a very nice formalization in terms of the index space[35] of the cells.

Implementing cell lists as described makes computing pair interactions scale better, but not without introducing a considerable constant factor. We can get around this problem by building the cell lists once at the very beginning and only rebuilding them if the particles travel beyond the maximum safe displacement

$$\Delta x^{\text{cell}} = \frac{l^{\text{cell}}}{2} - r^{\max}. \tag{99}$$

It is also possible to only check this condition occasionally, but doing so carries the risk of missing some of the interactions.

[34] The scaling follows the triangular number progression $N(N-1)/2$ for N particles.

[35] The index space is elaborated in appendix section G.

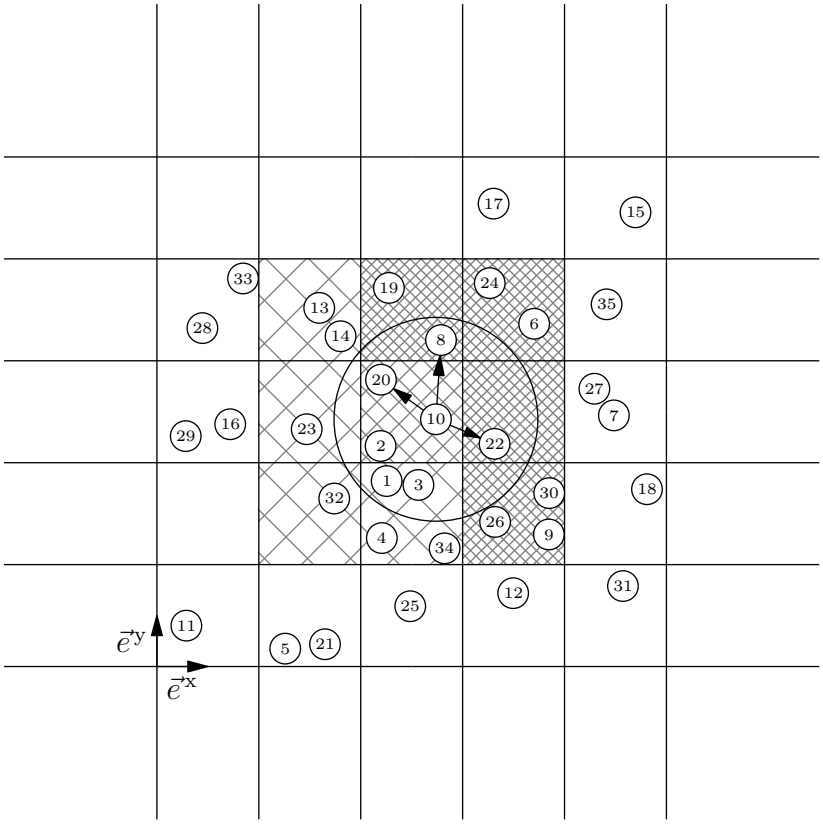

Figure 10: Sketch of leveraging cell lists to calculate the pair interactions of a particle. Periodic boundaries are not shown.

4.4.2 Parallel Processing

Cell lists decouple the processing of different parts of the system from each other, which makes them available for parallelization. However, since we need to run our simulation with several force models and vary the vertical target pressure as well, it is more effective to run each simulation in a separate process and let the operating system take care of the scheduling. This is not only easier to do, but also avoids the communication overhead that explicit parallelization would introduce.

5 Results and Analysis

We ran 75 simulations with 3 different force models and 25 different vertical target pressures. The force models were already discussed in section 3.4.2, but to reiterate, we used zero tangential forces for the case of no friction, HW for the case of dynamic friction and CS for the case of static and dynamic friction. The bounds of the vertical target pressures were also mentioned earlier, but it should be noted that since zero pressure is unattainable, we limited our sampling to $0.0125 \leq p^{\mathrm{driv}}/\sigma^{\mathrm{crit\,n}} \leq 1.0$.

5.1 Initial and Final States

Each simulation started from the same initial conditions, ran for $t^{\mathrm{fin}} - t^{\mathrm{init}} = (50.000 \pm 0.001)\,\mathrm{ms}$ and reached $\varepsilon = 1.00 \pm 0.01$ as expected. The simulations and their final states are summarized in table 1 with some of the final states also displayed in figure 11.

While looking at the final states does not tell the whole story, it does reveal that once the vertical target pressure exceeds $p^{\mathrm{driv}}/\sigma^{\mathrm{crit\,n}} = 0.6$, the fragment layer may reach the edges of the block. This can give rise to nonphysical effects due to the edges of the block being unbreakable, so we must reject such cases outright.

Looking at the final states also suggests that static friction may cause more elastic energy to build up, which, once released, facilitates the formation of cracks. Alas, it is difficult to tell whether this phenomenon is real or just an artifact of the calibration.

5.2 Dry Friction and Fragment Layer Growth

The coefficient of friction was estimated with equation 85. Since the equation depends on the components of $\vec{F}^{\mathrm{driv}}$, which may change at a rate of up to $100\,\mathrm{MN/s}$, the estimates featured a lot of noise. While a Savitzky–Golay filter was successful at eliminating the noise, it also distorted the data near the edges of its domain. We therefore opted to forgo the filtering and eliminate the noise by fitting the

Table 1: Informal summary of the simulations and their final states, where F indicates that there were more than a few fragments, C indicates that there were cracks that spanned more than a few particles, L indicates that fragments formed a layer that was thicker than a few particles, E indicates that the cracks that originated from the fragment layer reached the edges of the block and B indicates that the the fragment layer reached the edges of the block.

$p^{\text{driv}}/\sigma^{\text{crit n}}$	Zero					HW					CS				
0.0125											F				
0.025	F					F					F	C			
0.0375	F					F					F	C			
0.05	F					F					F	C			
0.0625	F					F					F				
0.075	F					F					F	C			
0.0875	F	C				F					F	C			
0.1	F	C	L			F					F	C	L		
0.1125	F	C				F					F	C	L		
0.125	F	C	L			F	C	L			F	C	L	E	
0.15	F	C	L			F	C	L			F	C	L	E	
0.175	F	C	L			F	C	L			F	C	L	E	
0.2	F	C	L			F	C	L			F	C	L	E	
0.225	F	C	L			F		L			F	C	L		
0.25	F	C	L			F		L			F	C	L		
0.3	F		L			F		L			F	C	L		
0.35	F		L			F	C	L			F	C	L		
0.4	F	C	L			F	C	L			F	C	L	E	
0.45	F	C	L			F	C	L			F	C	L	E	
0.5	F	C	L			F	C	L			F	C	L	E	
0.6	F	C	L	E		F	C	L	E		F	C	L	E	
0.7	F	C	L	E		F	C	L	E	B	F	C	L	E	
0.8	F	C	L	E		F	C	L	E	B	F	C	L	E	
0.9	F	C	L	E	B	F	C	L	E	B	F	C	L	E	B
1.0	F	C	L	E	B	F	C	L	E	B	F	C	L	E	B

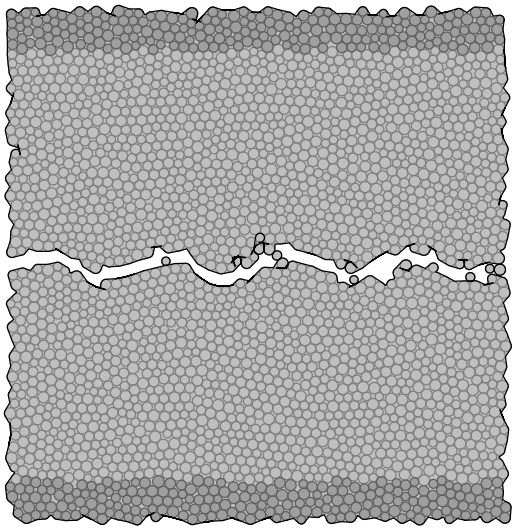

(a) Final state for HW at $p^{\mathrm{driv}}/\sigma^{\mathrm{crit\,n}} = 0.0125$. Very few fragments have broken off from the blocks.

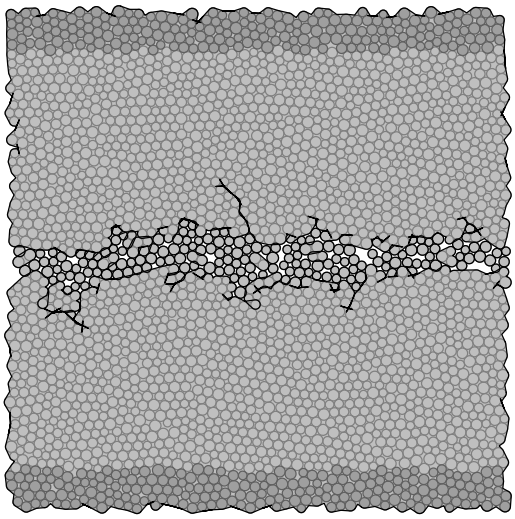

(b) Final state for HW at $p^{\mathrm{driv}}/\sigma^{\mathrm{crit\,n}} = 0.015$. The fragments have formed a thin layer.

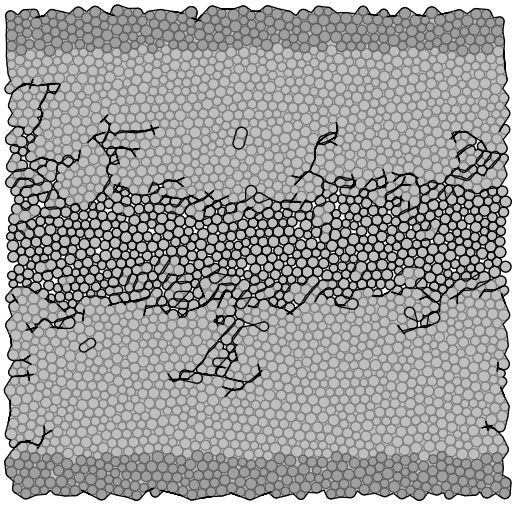

(c) Final state for HW at $p^{\mathrm{driv}}/\sigma^{\mathrm{crit\,n}} = 0.5$. The fragment layer has grown to be quite thick.

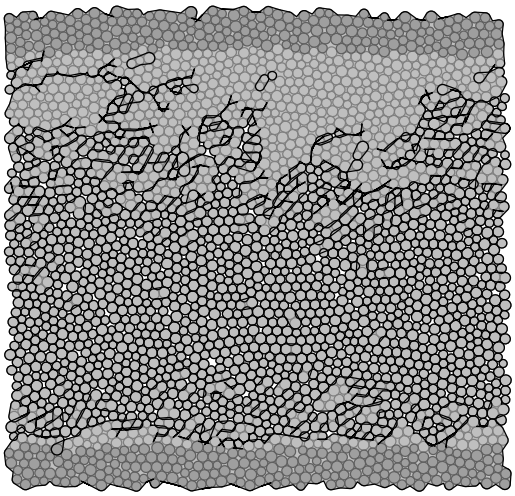

(d) Final state for HW at $p^{\mathrm{driv}}/\sigma^{\mathrm{crit\,n}} = 0.7$. The fragment layer has reached the edges of the block.

Figure 11: Sketches of the final states. Only some of the simulations are shown.

exponential[36] model

$$\mu = \begin{cases} (\mu^{\,\mathrm{crit}}/t^{\,\mathrm{crit}})t, & t \leq t^{\,\mathrm{crit}} \\ D_1 + (\mu^{\,\mathrm{crit}} - D_1)\exp(-D_2(t - t^{\,\mathrm{crit}})), & t \geq t^{\,\mathrm{crit}} \end{cases} \tag{100}$$

to the estimates, where $t^{\,\mathrm{crit}}$ and $\mu^{\,\mathrm{crit}}$ specify the point at which the initial static friction is overcome and D is free. Since this model has the limit

$$\lim_{t\to\infty} \mu = D_1, \tag{101}$$

we can interpret D_1 as the coefficient of friction for indefinitely large strains and D_2 as its decay constant. The fitting process and some of its results are presented in figure 12. A more comprehensive presentation of all the resulting coefficients of friction is in figure 13.

From figures 12 and 13 it is clear that the presence of internal friction has a substantial effect on the dry friction and a small effect on the growth rate of the fragment layer as well, although the particular force model in use does not seem to make much of a difference. The general trend is that the coefficient of friction increases with the internal friction while decreasing with the vertical target pressure. This trend does not manifest at very low or very high pressures, however.

At very low pressures there is no fragment layer to speak of, so the dry friction is almost completely determined by the roughness of the surfaces. Even if our fault was perfectly straight, the shapes of our particles would give rise to some roughness. A similar thing happens at very high pressures, where the fragment layer may grow almost indefinitely. After a certain point the fragments serve as a lubricant and the dry friction is primarily determined by the thickness of the fragment layer. Still, regardless of the pressure, the presence of internal friction strongly influences the mechanics inside the fragment layer. This is apparent in that increasing the internal friction makes the fragments roll past each other when they would otherwise be sliding.

[36] This model has no theoretical justification besides representing exponential decay and fitting the data really well.

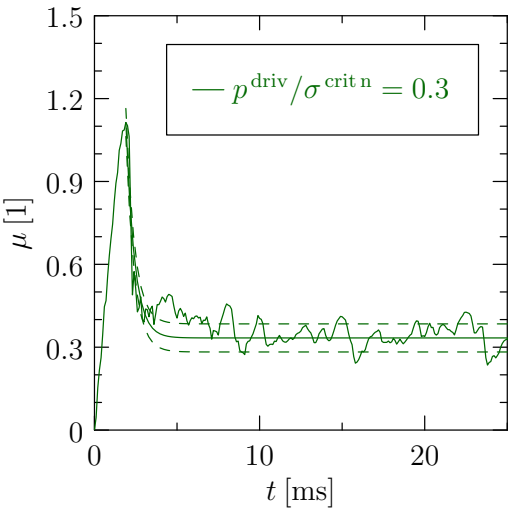

(a) Example of fitting for HW.

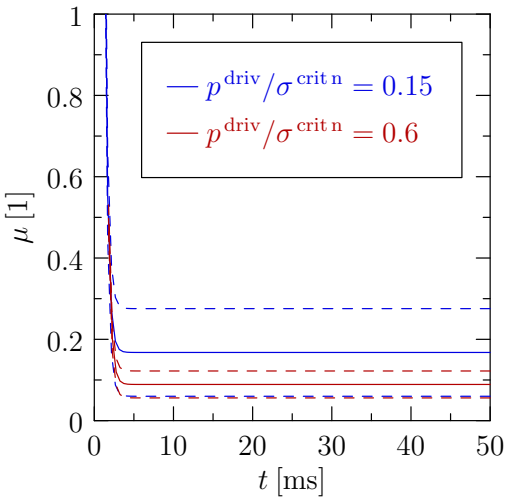

(b) Plot for zero friction.

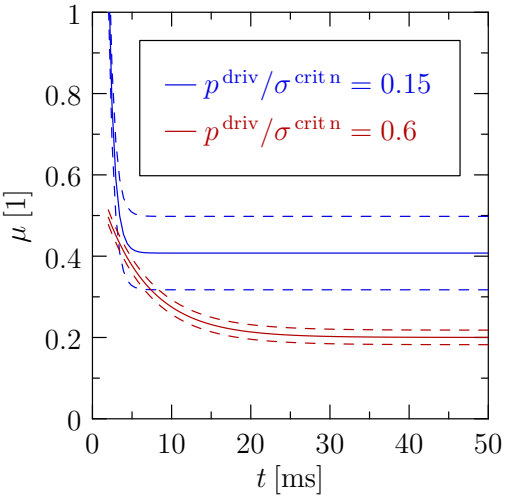

(c) Plot for HW.

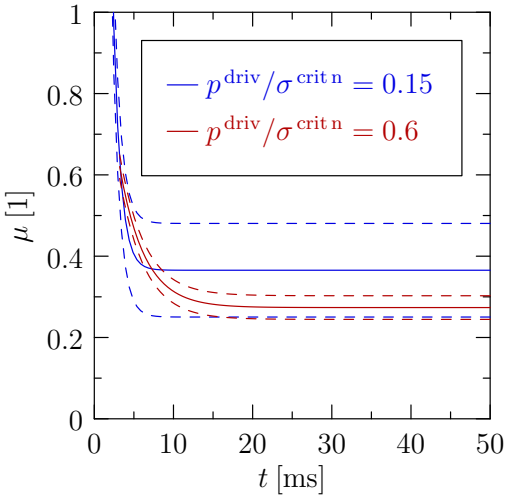

(d) Plot for CS.

Figure 12: Coefficient of friction μ as a function of time t and vertical target pressure p^{driv}. Only some of the simulations are shown. The solid lines represent the means and the dashed lines represent the standard deviations of the estimates.

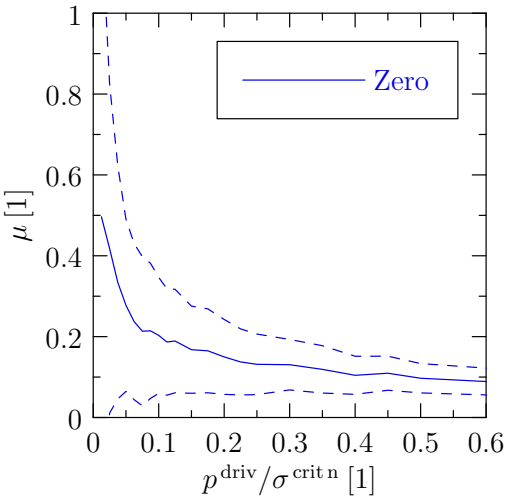

(a) Plot for zero friction.

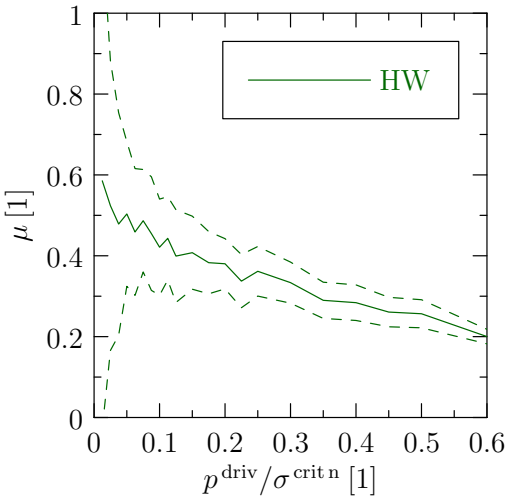

(b) Plot for HW.

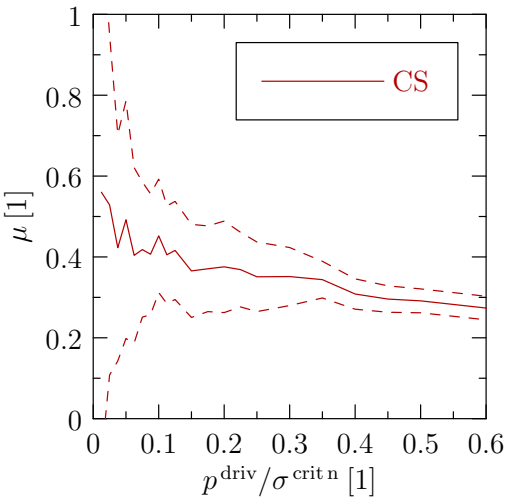

(c) Plot for CS.

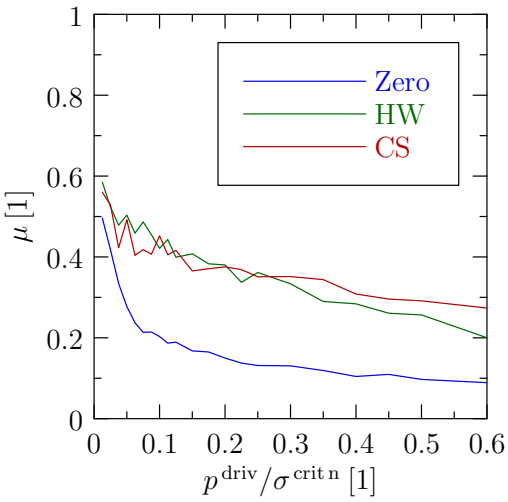

(d) Comparison of all the force models.

Figure 13: Coefficient of friction μ as a function of vertical target pressure p^{driv}. The solid lines represent the means and the dashed lines represent the standard deviations of the estimates.

5.3 Energy Dissipation

Energy conservation and dissipation were estimated with the equations presented in section 3.8.1. The energy drift was observed to be limited to 200 J/s in most cases, which is an acceptable margin for the conservation of energy. Figure 14 shows the energy dissipation curves for some of the simulations.

If fragmentation was not possible or the energy required to break the material into fragments matched the energy saved by the lubricating effect of the fragment layer, the energy dissipation would be directly proportional to the vertical target pressure. However, as figure 14 demonstrates, the energy dissipation increases significantly slower than a direct proportionality would predict. The practical consequence of this is that there is much less frictional heating when the fragments form a layer.

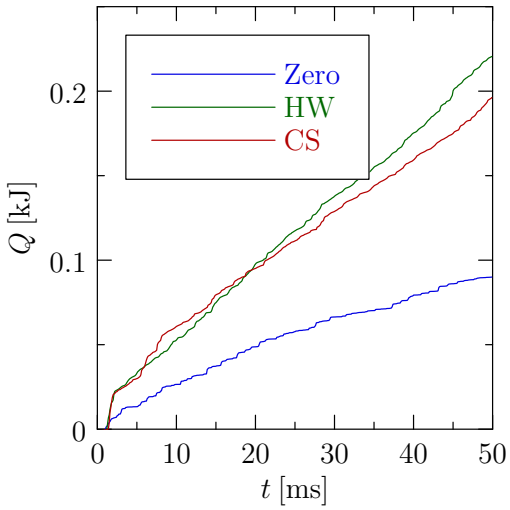

(a) Plot at $p^{\mathrm{driv}}/\sigma^{\mathrm{crit\,n}} = 0.075$.

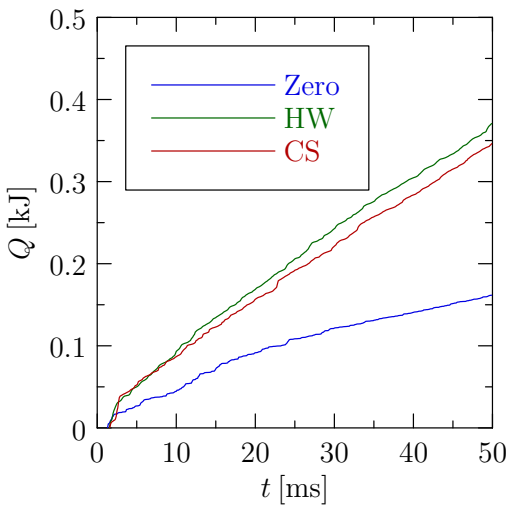

(b) Plot at $p^{\mathrm{driv}}/\sigma^{\mathrm{crit\,n}} = 0.15$.

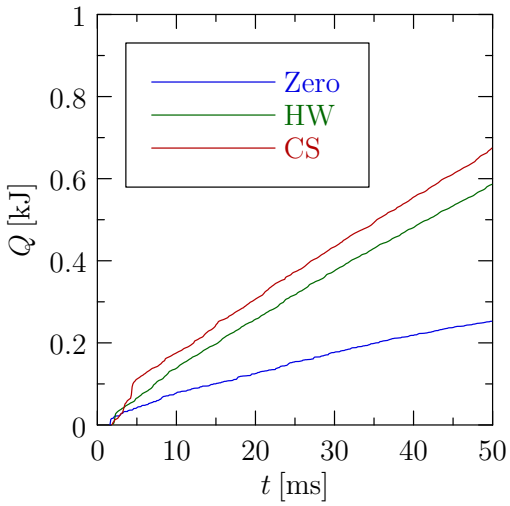

(c) Plot at $p^{\mathrm{driv}}/\sigma^{\mathrm{crit\,n}} = 0.3$.

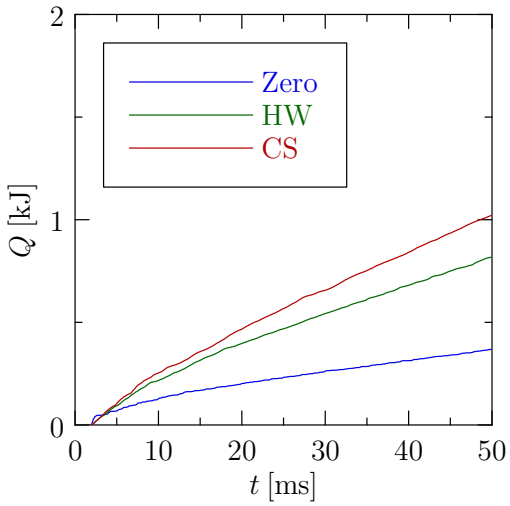

(d) Plot at $p^{\mathrm{driv}}/\sigma^{\mathrm{crit\,n}} = 0.6$.

Figure 14: Energy dissipation Q as a function of time t and vertical target pressure p^{driv}. Only some of the simulations are shown. The scales of the vertical axes are directly proportional to the vertical target pressures.

6 Conclusions

We investigated how different force models for internal friction affect dry friction and found that the effects are significant whenever the vertical pressure is within an order of magnitude from the ultimate strength of the material. Otherwise the dry friction is primarily determined by the roughness of the surfaces or the thickness of the fragment layer between them.

While our simulation allows the comparison of force models, it is almost certainly incapable of modeling the real behavior or granite. This could be improved by performing the calibration more rigorously, but there are a few other issues that potentially limit the effectiveness of this approach.

It is suspicious to use spherical particles, because granite powder typically contains a large amount of sharp-edged fragments. Even though the calibration can be adjusted to give spherical particles the same frictional properties that their sharp-edged counterparts would have, this is inelegant and physically questionable.

It is also suspicious to use a viscoelastic model, such as the one in equation 37, because the viscosity of granite is so large. Not only does the viscosity stretch the model over ten orders of magnitude beyond its typical range for fluids, it also causes problems with the numerical stability of the implementation.

Besides numerical stability, the implementation of CS proved to be quite problematic. Its definition in equation 42 contains two cases, one of which is completely conservative and the other of which is completely dissipative. Since the choice between the cases depends on $F_{i,j}^{\mathrm{n}}$, the model may quickly switch between the two. This makes the estimators in equations 76 and 78 report a huge energy drift even though the model is working as intended.

Aside from these shortcomings, we glossed over several questions that still remain open. What should the probability distribution of the link strength factor s be to reproduce any given strength distribution exactly? Would sharp-edged particles with simpler force models produce better results? How well would the model generalize to other brittle materials? Would the addition of water or some other surrounding medium change the behavior of the system markedly?

References

[1] L. da Vinci. *Codex Madrid*. Vol. 1. 1499.

[2] I. Newton. *Philosophiæ Naturalis Principia Mathematica*. Jussu Societatis Regiæ ac Typis Josephi Streater, 1687.

[3] G. Amontons. "Moyen de Substituer Commodément l'Action du Feu à la Force des Hommes et des Chevaux pour Mouvoir des Machines". In: *Mémoires de l'Académie Royale des Sciences*. Académie des Sciences, 1699-06-20, pp. 112–126.

[4] J. T. Desaguliers. *A Course of Experimental Philosophy*. Vol. 1. 1734.

[5] L. Euler. "Sur le Frottement des Corps Solides". In: *Mémoires de l'Académie des Sciences de Berlin*. Orell Füssli Turici, 1750, pp. 122–132.

[6] C.-A. de Coulomb. *Théorie des Machines Simples*. Bachelier, 1781.

[7] A. J. Morin. *Nouvelles Expériences sur le Frottement*. Vol. 1. Bachelier, 1832.

[8] O. Reynolds. "On the Theory of Lubrication and Its Application to Mr. Beauchamp Tower's Experiments, Including an Experimental Determination of the Viscosity of Olive Oil". In: *Philosophical Transactions of the Royal Society of London* 177 (1886), pp. 157–234.

[9] R. Stribeck. "Die wesentlichen Eigenschaften der Gleit- und Rollenlager". In: *Zeitschrift des Vereins Deutscher Ingenieure* 46.37 (1902), pp. 1341–1348.

[10] F. P. Bowden and D. Tabor. "The Area of Contact between Stationary and between Moving Surfaces". In: *Proceedings of the Royal Society of London A* 169.938 (1939), pp. 391–413.

[11] C. M. Mate et al. "Atomic-Scale Friction of a Tungsten Tip on a Graphite Surface". In: *Physical Review Letters* 59.17 (1987-10-26), pp. 1942–1945.

[12] H. Hertz. "Über die Berührung fester elastischer Körper". In: *Journal für die reine und angewandte Mathematik* 92 (1882), pp. 156–171.

[13] R. S. Bradley. “The Cohesive Force Between Solid Surfaces and the Surface Energy of Solids”. In: *The London, Edinburgh and Dublin Philosophical Magazine and Journal of Science* 13.86 (1932), pp. 853–862.

[14] K. L. Johnson, K. Kendall, and A. D. Roberts. “Surface Energy and the Contact of Elastic Solids”. In: *Proceedings of the Royal Society of London A* 324.1558 (1971), pp. 301–313.

[15] B. V. Derjaguin, V. M. Muller, and Y. P. Toporov. “Effect of Contact Deformations on the Adhesion of Particles”. In: *Journal of Colloid and Interface Science* 53.2 (1975), pp. 314–326.

[16] R. W. Carpick, D. F. Ogletree, and M. Salmeron. “A General Equation for Fitting Contact Area and Friction vs Load Measurements”. In: *Journal of Colloid and Interface Science* 211.2 (1999-03-15), pp. 395–400.

[17] J. J. Kalker. “On the Rolling Contact of Two Elastic Bodies in the Presence of Dry Friction”. PhD thesis. Delft University of Technology, 1967-07-05. URL: `http://resolver.tudelft.nl/uuid:aa44829b-c75c-4abd-9a03-fec17e121132`.

[18] C. E. Inglis. “Stresses in a Plate Due to the Presence of Cracks and Sharp Corners”. In: *Transactions of the Institute of Naval Architects* 55.219-241 (1913-03-14), pp. 193–198.

[19] A. A. Griffith. “The Phenomena of Flow and Rupture in Solids”. In: *Philosophical Transactions of the Royal Society of London* 221.A (1921-10-21), pp. 163–98.

[20] G. R. Irwin. “Analysis of Stresses and Strains near the End of a Crack Traversing a Plate”. In: *Journal of Applied Mechanics* 24.3 (1957-06), pp. 361–364.

[21] P. H. Jost. *Lubrication (Tribology), Education and Research: A Report on the Present Position and Industry’s Needs*. HM Stationery Office, 1966.

[22] J. T. Burwell. “Survey of Possible Wear Mechanisms”. In: *Wear* 1.2 (1957-10), pp. 119–141.

[23] L. F. Richardson. *Numerical Prediction by Numerical Processes*. Cambridge University Press, 1922.

[24] R. Courant, K. Friedrichs, and H. Lewy. “Über die partiellen Differenzengleichungen der mathematischen Physik”. In: *Mathematische Annalen* 100.1 (1928), pp. 32–74.

[25] R. Courant. “Variational Methods for the Solution of Problems of Equilibrium and Vibrations”. In: *Bulletin of the American Mathematical Society* 49 (1943), pp. 1–23.

[26] E. Fermi, J. Pasta, and S. Ulam. *Studies of Nonlinear Problems. Los Alamos Report LA-1940*. Los Alamos Laboratory, 1955.

[27] B. J. Alder and T. E. Wainwright. “Studies in Molecular Dynamics. I. General Method”. In: *The Journal of Chemical Physics* 31.2 (1959), pp. 459–466.

[28] P. A. Cundall. “A Computer Model for Simulating Progressive, Large-Scale Movements in Blocky Rock Systems”. In: *Proceedings of the International Symposium on Rock Mechanics*. Vol. 1. Ecole Nationale Supérieure de Géologie Appliquée et de Propsection Minière / Ecole Nationale Supérieure de la Métallurgie et de l’Industrie des Mines. Nancy, France, 1971-09, pp. II–8.

[29] P. A. Cundall and O. D. L. Strack. “A Discrete Numerical Model for Granular Assemblies”. In: *Géotechnique* 29.1 (1979-03), pp. 47–65.

[30] J. R. Williams, G. Hocking, and G. G. W. Mustoe. “The Theoretical Basis of the Discrete Element Method”. In: *Proceedings of the NUMETA ’85 Conference*. NUMETA: Numerical Methods of Engineering, Theory and Applications. Swansea, United Kingdom, 1985-01, pp. 897–906.

[31] G.-H. Shi and R. E. Goodman. “Two Dimensional Discontinuous Deformation Analysis”. In: *International Journal for Numerical and Analytical Methods in Geomechanics* 9.6 (1985), pp. 541–556.

[32] L. Jing. “Numerical Modelling of Jointed Rock Masses by Distinct Element Method for Two- and Three-Dimensional Problems”. PhD thesis. Luleøa Tekniska Universitet, 1990-10. URL: `http://www.diva-portal.org/smash/record.jsf?pid=diva2:990899`.

[33] C. W. Boon. “Distinct Element Modelling of Jointed Rock Masses: Algorithms and Their Verification”. PhD thesis. University of Oxford, 2013. URL: `http://www.eng.ox.ac.uk/civil/publications/theses/boon-1`.

[34] T. Riikilä. “Discrete Element Model for Viscoelastic Materials with Brittle Fracture: Applications on Glacier Dynamics”. PhD thesis. University of Jyväskylä, 2017-01-27. URL: https://jyx.jyu.fi/dspace/handle/123456789/52735.

[35] Z. Ning et al. “Distinct Element Simulation of Impact Breakage of Lactose Agglomerates”. In: *Advanced Powder Technology* 8.1 (1997), pp. 15–37.

[36] M. F. H. Wolff et al. “Three-Dimensional Discrete Element Modeling of Micromechanical Bending Tests of Ceramic–Polymer Composite Materials”. In: *Powder Technology* 248.Supplement C (2013-11). Discrete Element Modelling, pp. 77–83.

[37] C.-Y. Wu and A. C. F. Cocks. “Numerical and Experimental Investigations of the Flow of Powder into a Confined Space”. In: *Mechanics of Materials* 38.4 (2006-04), pp. 304–324.

[38] C. Thornton. “Numerical Simulations of Deviatoric Shear Deformation of Granular Media”. In: *Géotechnique* 50.1 (2000), pp. 43–53.

[39] A. Munjiza, D. R. J. Owen, and N. Bicanic. “A Combined Finite-Discrete Element Method in Transient Dynamics of Fracturing Solids”. In: *Engineering Computations* 12.2 (1995), pp. 145–174.

[40] J. Ai et al. “Assessment of Rolling Resistance Models in Discrete Element Simulations”. In: *Powder Technology* 206.3 (2011-01-30), pp. 269–282.

[41] Y. Li, Y. Xu, and C. Thornton. “A Comparison of Discrete Element Simulations and Experiments for ‘Sandpiles’ Composed of Spherical Particles”. In: *Powder Technology* 160.3 (2005-12-13), pp. 219–228.

[42] B. K. Mishra and R. K. Rajamani. “The Discrete Element Method for the Simulation of Ball Mills”. In: *Applied Mathematical Modelling* 16.11 (1992-11), pp. 598–604.

[43] P. W. Cleary and M. L. Sawley. “DEM Modelling of Industrial Granular Flows: 3D Case Studies and the Effect of Particle Shape on Hopper Discharge”. In: *Applied Mathematical Modelling* 26.2 (2002-02), pp. 89–111.

[44] T. Bym et al. “Use of a Two-Dimensional Discrete-Element Line-Sink Model to Gain Insight into Tunnelling-Induced Deformations”. In: *Géotechnique* 63.9 (2013), p. 791.

[45] D. Elmo et al. “Applications of Finite/Discrete Element Modeling to Rock Engineering Problems”. In: *International Journal of Geomechanics* 13.5 (2013), pp. 565–580.

[46] W. R. Ketterhagen, M. T. am Ende, and B. C. Hancock. “Process Modeling in the Pharmaceutical Industry Using the Discrete Element Method”. In: *Journal of Pharmaceutical Sciences* 98.2 (2009-02), pp. 442–470.

[47] M. V. Zeebroeck. “The Discrete Element Method (DEM) to Simulate Fruit Impact Damage during Transport and Handling”. PhD thesis. Katholieke Universiteit Leuven, 2005-04-22. URL: `https://lirias.kuleuven.be/handle/1979/46`.

[48] J. M. Boac et al. “Applications of Discrete Element Method in Modeling of Grain Postharvest Operations”. In: *Food Engineering Reviews* 6.4 (2014-12-01), pp. 128–149.

[49] E. Coumans et al. *Bullet*. 2017-09-29. URL: `http://bulletphysics.org/`.

[50] E. Catto. *Box2D*. 2013-11-03. URL: `http://box2d.org/`.

[51] G. W. Leibniz. *Nova Methodus pro Maximis et Minimis*. Acta Eruditorum, 1684.

[52] N. P. Petrov. “Friction in Machines and the Effect of Lubricant”. In: *Engineering Journal of Saint Petersburg* 1 (1883), pp. 71–140.

[53] D. Maugis. “Adhesion of Spheres: The JKR–DMT Transition Using a Dugdale Model”. In: *Journal of Colloid and Interface Science* 150.1 (1992-04), pp. 243–269.

[54] D. Dowson. *History of Tribology*. 2nd ed. Wiley, 1998-01.

[55] S. G. Nash. *A History of Scientific Computing*. Association for Computing Machinery, 1990.

[56] I. M. Hutchings. “Leonardo da Vinci’s Studies of Friction”. In: *Wear* 360 (2016-08-15), pp. 51–66.

[57] V. Thomée. “From Finite Differences to Finite Elements: A Short History of Numerical Analysis of Partial Differential Equations”. In: *Journal of Computational and Applied Mathematics* 128.1–2 (2001-03-01), pp. 1–54.

[58] P. Mora and D. Place. “Simulation of the Frictional Stick-Slip Instability”. In: *Pure and Applied Geophysics* 143.1 (1994-03), pp. 61–87.

[59] P. Mora and D. Place. “Numerical Simulation of Earthquake Faults with Gouge: Toward a Comprehensive Explanation for the Heat Flow Paradox”. In: *Journal of Geophysical Research: Solid Earth* 103.B9 (1998-09-10), pp. 21067–21089.

[60] D. R. Scott, C. J. Marone, and C. G. Sammis. “The Apparent Friction of Granular Fault Gouge in Sheared Layers”. In: *Journal of Geophysical Research: Solid Earth* 99.B4 (1994-04-10), pp. 7231–7246.

[61] N. M. Beeler et al. “Frictional Behavior of Large Displacement Experimental Faults”. In: *Journal of Geophysical Research: Solid Earth* 101.B4 (1996-04-10), pp. 8697–8715.

[62] J. Schäfer, S. Dippel, and D. Wolf. “Force Schemes in Simulations of Granular Materials”. In: *Journal de Physique I* 6.1 (1996-01-01), pp. 5–20. URL: `https://hal.archives-ouvertes.fr/jpa-00247176`.

[63] A. Fakhimi and T. Villegas. “Application of Dimensional Analysis in Calibration of a Discrete Element Model for Rock Deformation and Fracture”. In: *Rock Mechanics and Rock Engineering* 40.2 (2006-06-09), pp. 193–211.

[64] A. H. Lachenbruch and J. H. Sass. “The Stress Heat-Flow Paradox and Thermal Results from Cajon Pass”. In: *Geophysical Research Letters* 15.9 (1988-08), pp. 981–984.

[65] S. I. Henderson et al. “Effect of Particle Size Distribution on Crystallisation and the Glass Transition of Hard Sphere Colloids”. In: *Physica A: Statistical Mechanics and its Applications* 233.1 (1996-11-15), pp. 102–116.

[66] Merriam–Webster. *“stiction”*. 2012-02-02. URL: `https://www.merriam-webster.com/dictionary/stiction`.

[67] O. Ben-David and J. Fineberg. “Static Friction Coefficient Is Not a Material Constant”. In: *Physical Review Letters* 106.25 (2011-06-24), p. 254301.

[68] Z. Deng et al. “Adhesion-Dependent Negative Friction Coefficient on Chemically Modified Graphite at the Nanoscale”. In: *Nature Materials* 11.12 (2012-12-01), pp. 1032–1037.

[69] J. Byerlee. “Friction of Rocks”. In: *Pure and Applied Geophysics* 116.4 (1978-07-01), pp. 615–626.

[70] W. Goldsmith, J. L. Sackman, and C. Ewerts. “Static and Dynamic Fracture Strength of Barre Granite”. In: *International Journal of Rock Mechanics and Mining Sciences* 13.11 (1976-11), pp. 303–309.

[71] N. Kumagai, S. Sasajima, and H. Ito. “Long-Term Creep of Rocks: Results with Large Specimens Obtained in about 20 Years and Those with Small Specimens in about 3 Years”. In: *Journal of the Society of Materials Science* 27.293 (1978), pp. 155–161.

[72] K. J. R. Rasmussen. “Full-Range Stress–Strain Curves for Stainless Steel Alloys”. In: *Journal of Constructional Steel Research* 59.1 (2003-01), pp. 47–61.

[73] R. Mittal and S. Balachandar. “Effect of Three-Dimensionality on the Lift and Drag of Nominally Two-Dimensional Cylinders”. In: *Physics of Fluids* 7.8 (1995-08), pp. 1841–1865.

[74] N. V. Brilliantov et al. “Model for Collisions in Granular Gases”. In: *Physical Review E* 53.5 (1996-05-01), pp. 5382–5392.

[75] T. Pöschel and V. Buchholtz. “Molecular Dynamics of Arbitrarily Shaped Granular Particles”. In: *Journal de Physique I* 5.11 (1995), pp. 1431–1455.

[76] S. M. Han, H. Benaroya, and T. Wei. “Dynamics of Transversely Vibrating Beams Using Four Engineering Theories”. In: *Journal of Sound and Vibration* 225.5 (1999-09-02), pp. 935–988.

[77] Z. F. Zhang and J. Eckert. “Unified Tensile Fracture Criterion”. In: *Physical Review Letters* 94.9 (2005-03-11), p. 094301.

[78] H. Kruggel-Emden et al. “Review and Extension of Normal Force Models for the Discrete Element Method”. In: *Powder Technology* 171.3 (2007-02-26), pp. 157–173.

[79] F. A. Morrison. *An Introduction to Fluid Mechanics*. 1st ed. Cambridge University Press, 2013.

[80] A. Hölzer and M. Sommerfeld. “New Simple Correlation Formula for the Drag Coefficient of Non-Spherical Particles”. In: *Powder Technology* 184.3 (2008-06-02), pp. 361–365.

[81] S. B. Chen and X. Ye. “Faxen’s Laws of a Composite Sphere under Creeping Flow Conditions”. In: *Journal of Colloid and Interface Science* 221.1 (2000-01-01), pp. 50–57.

[82] N. V. Brilliantov and T. Pöschel. “Rolling Friction of a Viscous Sphere on a Hard Plane”. In: *Europhysics Letters* 42.5 (1998-06-01), pp. 511–516.

[83] J. Lee and H. J. Herrmann. “Angle of Repose and Angle of Marginal Stability: Molecular Dynamics of Granular Particles”. In: *Journal of Physics A: Mathematical and General* 26.2 (1993), pp. 373–383.

[84] P. M. Amaral, J. C. Fernandes, and L. G. Rosa. “Weibull Statistical Analysis of Granite Bending Strength”. In: *Rock Mechanics and Rock Engineering* 41.6 (2008-12-01), pp. 917–928.

[85] L. Afferrante, M. Ciavarella, and E. Valenza. “Is Weibull’s Modulus Really a Material Constant? Example Case with Interacting Collinear Cracks”. In: *International Journal of Solids and Structures* 43.17 (2006-08), pp. 5147–5157.

[86] P. Bak, C. Tang, and K. Wiesenfeld. “Self-Organized Criticality”. In: *Physical Review A* 38.1 (1988-07-01), pp. 364–374.

[87] H. Kruggel-Emden et al. “Selection of an Appropriate Time Integration Scheme for the Discrete Element Method (DEM)”. In: *Computers and Chemical Engineering* 32.10 (2008-10-17), pp. 2263–2279.

[88] A. A. Kuraev et al. “Fast Algorithm for Numerically Integrating Equations of Motion for Large Particles in Microwave Devices”. In: *Technical Physics* 59.3 (2014-03-01), pp. 318–324.

[89] C. O’Sullivan and J. D. Bray. “Selecting a Suitable Time Step for Discrete Element Simulations That Use the Central Difference Time Integration Scheme”. In: *Engineering Computations* 21.2/3/4 (2004), pp. 278–303.

[90] P. A. Thompson and G. S. Grest. “Granular Flow: Friction and the Dilatancy Transition”. In: *Physical Review Letters* 67.13 (1991-09-23), pp. 1751–1754.

[91] S. Winkler, D. A. Shockey, and D. R. Curran. “Crack Propagation at Supersonic Velocities, I”. In: *International Journal of Fracture Mechanics* 6.2 (1970-06-01), pp. 151–158.

[92] D. R. Curran, D. A. Shockey, and S. Winkler. “Crack Propagation at Supersonic Velocities, II”. In: *International Journal of Fracture Mechanics* 6.3 (1970-09-01), pp. 271–278.

[93] S. Torquato, T. M. Truskett, and P. G. Debenedetti. “Is Random Close Packing of Spheres Well Defined?” In: *Physical Review Letters* 84.10 (2000-03-06), pp. 2064–2067.

[94] W. M. Visscher and M. Bolsterli. “Random Packing of Equal and Unequal Spheres in Two and Three Dimensions”. In: *Nature* 239.5374 (1972-10-27), pp. 504–507.

[95] J. Tobochnik and P. M. Chapin. “Monte Carlo Simulation of Hard Spheres Near Random Closest Packing Using Spherical Boundary Conditions”. In: *The Journal of Chemical Physics* 88.9 (1988-05-01), pp. 5824–5830.

[96] T. M. Truskett, S. Torquato, and P. G. Debenedetti. “Towards a Quantification of Disorder in Materials: Distinguishing Equilibrium and Glassy Sphere Packings”. In: *Physical Review E* 62.1 (2000-07-01), pp. 993–1001.

[97] S. Strobl, A. Formella, and T. Pöschel. “Exact Calculation of the Overlap Volume of Spheres and Mesh Elements”. In: *Journal of Computational Physics* 311 (2016), pp. 158–172.

[98] S. Kiiskinen. *Brittle Matter Matters*. 2018-01-22. URL: `http://users.jyu.fi/~sapekiis/brittle-matter-matters/`.

[99] S. Abe et al. *ESyS-Particle*. 2017-01-06. URL: `https://www.uio.no/english/services/it/research/hpc/abel/help/software/ESyS-Particle.html`.

[100] V. Šmilauer et al. *Yade*. 2017-01-19. URL: `https://yade-dem.org/doc/`.

[101] C. Kloss et al. *LIGGGHTS*. 2017-10-01. URL: `https://www.cfdem.com/`.

[102] R. A. Daly. “Densities of Rocks Calculated from Their Chemical Analyses”. In: *Proceedings of the National Academy of Sciences* 21.12 (1935), pp. 657–663.

[103] J. M. Ide. “Comparison of Statically and Dynamically Determined Young’s Modulus of Rocks”. In: *Proceedings of the National Academy of Sciences* 22.2 (1936), pp. 81–92.

[104] H. Gercek. “Poisson’s Ratio Values for Rocks”. In: *International Journal of Rock Mechanics and Mining Sciences* 44.1 (2007-01), pp. 1–13.

[105] W. Sutherland. “LII. The Viscosity of Gases and Molecular Force”. In: *The London, Edinburgh and Dublin Philosophical Magazine and Journal of Science* 36.223 (1893), pp. 507–531.

[106] R. Ramírez et al. “Coefficient of Restitution of Colliding Viscoelastic Spheres”. In: *Physical Review E* 60.4 (1999-10-01), pp. 4465–4472.

[107] D. D. Durda et al. “Experimental Determination of the Coefficient of Restitution for Meter-Scale Granite Spheres”. In: *Icarus* 211.1 (2011-01), pp. 849–855.

[108] J. H. Conway and N. J. A. Sloane. *Sphere Packings, Lattices and Groups*. 3rd ed. Springer, 1998.

A Summary of Notational Conventions

Tables 2, 3 and 4 summarize the notational conventions used throughout this work. Notable deviations from literature include η instead of μ for viscosity, Υ instead of ε for the coefficient of restitution, q instead of η for the packing fraction, Λ instead of A for the dissipative constant and β instead of α for the axial ratio.

Table 2: Notational conventions used throughout this work with Greek letters sorted by Beta Code. This table only covers uppercase symbols; lowercase symbols are in table 3 and keywords are in table 4.

A	Area		
B	Statistical Bandwidth		
C	Drag Coefficient	Ξ	Adjusted Normal Displacement
D	Dimensionless Constant	Δ	Difference
E	Energy		
F	Force	Φ	Particle Sphericity
G	Shear Modulus		
J	Moment of Inertia		
K	Bulk Modulus		
L	Characteristic Length	Λ	Dissipative Constant
M	P-Wave Modulus		
N	Number of Particles		
P	Probability Density	Π	Product
Q	Heat	Ψ	Statistical Kernel
R	Characteristic Radius		
S	Two-Body Excess Entropy	Σ	Sum
T	Characteristic Duration		
U	External Potential	Υ	Coefficient of Restitution
V	Volume		
W	Work		
X	Magnification		
Y	Young's Modulus		
Z	Normalization Constant		

Table 3: Notational conventions used throughout this work with Greek letters sorted by Beta Code. This table only covers lowercase symbols; uppercase symbols are in table 2 and keywords are in table 4.

a	Particle Acceleration	α	Particle Angular Acceleration
b	Overlap Factor	β	Axial Ratio
c	Wave Speed	ξ	Normal Displacement
d	Distance	δ	Indicator Function
e	Basis Component	ε	Strain
f	Frequency	φ	Particle Angular Displacement
g	Radial Distribution	γ	Calibration Parameter
h	Height of Jags	θ	Central Angle
i	Particle Index		
j	Particle Index		
k	Weibull Modulus	$\varkappa$	Potential Strength
l	Length	λ	Frame Angular Displacement
m	Mass	μ	Coefficient of Friction
n	Number of Jags	ν	Poisson's Ratio
o	Focal Point		
p	Pressure	π	Mathematical Constant
q	Packing Fraction	ψ	Relative Angular Displacement
r	Particle Radius	ρ	Density
s	Link Strength Factor	σ	Stress
t	Time	τ	Torque
u	Average Contact Distance		
v	Particle Velocity		
w	Statistical Weight	ω	Particle Angular Velocity
x	Particle Displacement		
y	Minimum Contact Distance	η	Viscosity
z	Contact Half-Length	ζ	Tangential Displacement

Table 4: Notational conventions used throughout this work with concepts roughly sorted by similarity. This table only covers keywords; symbols are in tables 2 and 3.

aKV	Adjusted Kelvin–Voigt	EB	Euler–Bernoulli
bond	Bonding	brk	Breaking
cell	Cell	cut	Cutoff
cont	Contact	fric	Frictional
crit	Critical	avg	Average
ext	External	driv	Driven
HW	Haff–Werner	CS	Cundall–Strack
init	Initial	fin	Final
KV	Kelvin–Voigt	BSHP	Brilliantov–Spahn–Hertzsch–Pöschel
kin	Kinetic	amb	Ambient
min	Minimum	max	Maximum
n	Normal	t	Tangential
P	Primary	S	Secondary
pred	Predicted	corr	Corrected
Re	Reynolds Number	Ma	Mach Number
rev	Reverse	per	Perpendicular
x	Horizontal	y	Vertical
z	Depthwise	B	Boltzmann

B Approximating the Number of Particles

Let us consider a periodic d-dimensional system consisting of a hypercube with side length L that is optimally packed with hyperspherical particles with radius R. The number of particles in the system

$$N_d = q_d \frac{V_d^{\square}}{V_d^{\bigcirc}}, \tag{102}$$

where q is the packing fraction, $V^{\square}$ is the volume of the hypercube and $V^{\bigcirc}$ is the volume of a hypersphere.

There is more to equation 102 than meets the eye [108], but for our needs it is sufficient to note that it has a closed form in both two and three dimensions. In two dimensions

$$q_2 = \frac{(2\pi)}{4\sqrt{3}} \qquad V_2^{\square} = L^2 \qquad V_2^{\bigcirc} = \frac{(2\pi)}{2} R^2 \qquad N_2 = \frac{1}{2\sqrt{3}} \left(\frac{L}{R}\right)^2 \tag{103}$$

while in three dimensions

$$q_3 = \frac{(2\pi)}{6\sqrt{2}} \qquad V_3^{\square} = L^3 \qquad V_3^{\bigcirc} = \frac{2\,(2\pi)}{3} R^3 \qquad N_3 = \frac{1}{4\sqrt{2}} \left(\frac{L}{R}\right)^3. \tag{104}$$

The ratio

$$\frac{N_3}{N_2} = \frac{\sqrt{6}}{4} \left(\frac{L}{R}\right) \tag{105}$$

tells us the scale factor for the number of particles when going from two to three dimensions. The ratio is obviously different for a suboptimal packing like the isotropic material we study in this work, but this result for the worst case is still a useful approximation.

C Properties of the Inverse Tangent

We define the inverse tangent for vector arguments such that

$$\arctan \begin{bmatrix} \cos x \\ \sin x \end{bmatrix} = x \tag{106}$$

for all x satisfying $|x| \leq (2\pi)/2$. This can be accomplished with the explicit definition

$$\arctan \begin{bmatrix} x^{\mathrm{x}} \\ x^{\mathrm{y}} \end{bmatrix} = \begin{cases} \arctan |x^{\mathrm{y}}/x^{\mathrm{x}}|, & x^{\mathrm{x}} > 0, x^{\mathrm{y}} > 0 \\ 0, & x^{\mathrm{x}} > 0, x^{\mathrm{y}} = 0 \\ -\arctan |x^{\mathrm{y}}/x^{\mathrm{x}}|, & x^{\mathrm{x}} > 0, x^{\mathrm{y}} < 0 \\ (2\pi)/4, & x^{\mathrm{x}} = 0, x^{\mathrm{y}} > 0 \\ \perp, & x^{\mathrm{x}} = 0, x^{\mathrm{y}} = 0 \\ -(2\pi)/4, & x^{\mathrm{x}} = 0, x^{\mathrm{y}} < 0 \\ -\arctan |x^{\mathrm{y}}/x^{\mathrm{x}}| + (2\pi)/2, & x^{\mathrm{x}} < 0, x^{\mathrm{y}} > 0 \\ \pm (2\pi)/2, & x^{\mathrm{x}} < 0, x^{\mathrm{y}} = 0 \\ \arctan |x^{\mathrm{y}}/x^{\mathrm{x}}| - (2\pi)/2, & x^{\mathrm{x}} < 0, x^{\mathrm{y}} < 0 \end{cases} \tag{107}$$

for all $\vec{x}$ satisfying $\vec{x} \neq \vec{0}$.

The inverse tangent has a couple of notable properties we make use of. The first one says that reversing its argument reverses the resulting angle, as in

$$\arctan -\vec{x} = \operatorname{rev} \arctan \vec{x}, \tag{108}$$

where

$$\operatorname{rev} x = \begin{cases} x - (2\pi)/2, & x > 0 \\ \pm (2\pi)/2, & x = 0 \\ x + (2\pi)/2, & x < 0 \end{cases} \tag{109}$$

for all x satisfying $|x| \leq (2\pi)/2$. The second one says that its derivative is equivalent to a function that produces a scaled perpendicular, that is,

$$\vec{\nabla} \arctan \vec{x} = \operatorname{per} \frac{\vec{x}}{|\vec{x}|^2}, \tag{110}$$

where taking the perpendicular is performed with

$$\text{per} \begin{bmatrix} x^{\text{x}} \\ x^{\text{y}} \end{bmatrix} = \begin{bmatrix} -x^{\text{y}} \\ x^{\text{x}} \end{bmatrix} \tag{111}$$

for all $\vec{x}$.

D Contact Point of Two Particles

In section 3.3.1 we assumed that particles are in contact when they overlap, but did not calculate the actual contact geometry or explain how it is compatible with the concept of point forces. Let us address these concerns.

Given two different particles indexed with i and j, the distance of i from their focal point

$$y_{i,j} = b_{i,j}|\vec{x}_j - \vec{x}_i|. \tag{112}$$

Applying the Pythagorean theorem to this produces the half-length of the contact

$$z_{i,j} = \sqrt{r_i^2 - y_{i,j}^2} = z_{j,i}. \tag{113}$$

The actual distance from the contact varies between r_i and $y_{i,j}$, so it cannot be given a single value. We can, however, calculate its average along the length of the contact as

$$\begin{aligned} u_{i,j} &= \frac{1}{2z_{i,j}} \int_{-z_{i,j}}^{z_{i,j}} \mathrm{d}z \, \sqrt{z^2 + y_{i,j}^2} = \frac{y_{i,j}}{2}\left(\sqrt{1 + \left(\frac{z_{i,j}}{y_{i,j}}\right)^2} + \frac{y_{i,j}}{z_{i,j}} \operatorname{arsinh} \frac{z_{i,j}}{y_{i,j}}\right) \\ &= \frac{y_{i,j}}{2}\left(\frac{r_i}{y_{i,j}} + \frac{\operatorname{arsinh} \sqrt{(r_i/y_{i,j})^2 - 1}}{\sqrt{(r_i/y_{i,j})^2 - 1}}\right). \end{aligned} \tag{114}$$

The resulting expression is quite complicated, but we may simplify it considerably by replacing the trigonometric function with its Taylor series up to second order. This procedure yields the approximation

$$u_{i,j} = \frac{r_i + y_{i,j}}{2}, \tag{115}$$

which is coincidentally the arithmetic mean of the extremities.

Now, if the contact area is very small, we may safely assume that the contact point is at distance r_i from i. Otherwise we may have to adjust the distance to $y_{i,j}$ or $u_{i,j}$. If neither option was satisfactory, we would have to base our calculations directly on the contact area

$$A_{i,j} = \frac{(2\pi)}{2} z_{i,j}^2 = A_{j,i} \tag{116}$$

or the displaced volume

$$\begin{aligned} V_{i,j} &= \frac{(2\pi)}{3}(r_i - y_{i,j})r_i^2 - \frac{(2\pi)}{6}y_{i,j}z_{i,j}^2 + \frac{(2\pi)}{3}(r_j - y_{j,i})r_j^2 - \frac{(2\pi)}{6}y_{j,i}z_{j,i}^2 \\ &= \frac{(2\pi)}{6}(2r_i + y_{i,j})(r_i - y_{i,j})^2 + \frac{(2\pi)}{6}(2r_j + y_{j,i})(r_j - y_{j,i})^2 = V_{j,i}. \end{aligned} \tag{117}$$

In the case of cylindrical particles of depth L^{z}, the contact area would be

$$A_{i,j} = 2L^{\mathrm{z}}z_{i,j} = A_{j,i} \tag{118}$$

and the displaced volume would be

$$\begin{aligned} V_{i,j} &= \frac{1}{2}L^{\mathrm{z}}\theta_{i,j}r_i^2 - L^{\mathrm{z}}y_{i,j}z_{i,j} + \frac{1}{2}L^{\mathrm{z}}\theta_{j,i}r_j^2 - L^{\mathrm{z}}y_{j,i}z_{j,i} \\ &= \frac{1}{2}L^{\mathrm{z}}(\theta_{i,j}r_i^2 - 2y_{i,j}z_{i,j}) + \frac{1}{2}L^{\mathrm{z}}(\theta_{j,i}r_j^2 - 2y_{j,i}z_{i,j}) = V_{j,i}, \end{aligned} \tag{119}$$

where the central angles from particles i and j to the contact are

$$\theta_{i,j} = 2\arccos\frac{y_{i,j}}{r_i} \qquad\qquad \theta_{j,i} = 2\arccos\frac{y_{j,i}}{r_j} \tag{120}$$

respectively.

E Operations on Probability Distributions

Given two continuous random variables A and B with the probability densities P_A and P_B respectively, their sum and product distributions have the probability densities

$$\begin{aligned} P_{A+B}(x) &= \int_{-\infty}^{\infty} \mathrm{d}y\, P_A(y) P_B(x-y) \\ P_{AB}(x) &= \int_{-\infty}^{\infty} \mathrm{d}y\, \frac{P_A(y) P_B(x/y)}{|y|} \end{aligned} \tag{121}$$

respectively. Assuming A and B are independent and uniformly distributed, A in the proper interval from a to b and B in the proper interval from c to d, their sum distribution has the probability density

$$P_{A+B}(x) = \frac{1}{(b-a)(d-c)} \begin{cases} \mathrm{sum}_{c,d}^{a,b}(x), & a+d \le b+c \\ \mathrm{sum}_{a,b}^{c,d}(x), & a+d \ge b+c, \end{cases} \tag{122}$$

where

$$\mathrm{sum}_{a,b}^{c,d}(x) = \begin{cases} 0, & x \le a+c \\ x-(a+c), & a+c \le x \le b+c \\ b-a, & b+c \le x \le a+d \\ (b+d)-x, & a+d \le x \le b+d \\ 0, & b+d \le x. \end{cases} \tag{123}$$

Further assuming[37] that $a > 0$ and $c > 0$, their product distribution has the probability density

$$P_{AB}(x) = \frac{1}{(b-a)(d-c)} \begin{cases} \mathrm{prod}_{c,d}^{a,b}(x), & ad \le bc \\ \mathrm{prod}_{a,b}^{c,d}(x), & ad \ge bc, \end{cases} \tag{124}$$

[37] Getting rid of this assumption would be straightforward, but require four times as many case analyses.

where

$$\operatorname{prod}_{a,b}^{c,d}(x) = \begin{cases} 0, & x \le ac \\ \log x - (\log a + \log c), & ac \le x \le bc \\ \log b - \log a, & bc \le x \le ad \\ (\log b + \log d) - \log x, & ad \le x \le bd \\ 0, & bd \le x. \end{cases} \tag{125}$$

Given a continuous random variable C with the probability density P_C and a compatible invertible function f, the distribution of C transformed with f has the probability density

$$P_{f(C)}(x) = P_A\Big(f^{-1}(x)\Big)|\partial_x f^{-1}(x)|. \tag{126}$$

Assuming $C = AB$ and $f(x) = x^n$ for some $n > 0$, the transformed distribution has the probability density

$$P_{f(AB)}(x) = \frac{x^{(1-n)/n}/n}{(b-a)(d-c)} \begin{cases} \operatorname{prod}_{c,d}^{a,b}(x^{1/n}), & ad \le bc \\ \operatorname{prod}_{a,b}^{c,d}(x^{1/n}), & ad \ge bc. \end{cases} \tag{127}$$

F Bounding the Particle Size Distribution

Let A be a continuous random variable representing particle sizes. Assuming that A is uniformly distributed in the proper interval from a to b, its mean and standard deviation are

$$\mu = \frac{a+b}{2} \qquad\qquad \sigma = \frac{b-a}{2\sqrt{3}} \tag{128}$$

respectively. Inverting this system of equations gives us the expressions

$$a = \mu - \sigma\sqrt{3} \qquad\qquad b = \mu + \sigma\sqrt{3} \tag{129}$$

for the endpoints of the interval. If we assume that the transition condition

$$\frac{\sigma}{\mu} < 0.1 \tag{130}$$

from section 3.7.2 is barely satisfied with, say,

$$\frac{\sigma}{\mu} = \sqrt{3} - \frac{2\sqrt{6}}{3} \approx 0.99, \tag{131}$$

we can find the ratio

$$\frac{b}{a} = \frac{\mu + \sigma\sqrt{3}}{\mu - \sigma\sqrt{3}} = \frac{1/\sqrt{3} + \sigma/\mu}{1/\sqrt{3} - \sigma/\mu} = \sqrt{2} \tag{132}$$

and use it to obtain

$$a = \left(\frac{2}{1+\sqrt{2}}\right)\mu \qquad\qquad b = \left(\frac{4}{2+\sqrt{2}}\right)\mu. \tag{133}$$

We can now easily find the uniform distribution that is right on the verge of transition for any average particle size μ.

G Life in the Index Space

Let us briefly discuss the relation between the two-dimensional Euclidean space and the two-dimensional index space. The main difference between them is that the Euclidean space is defined over the real numbers while the index space is defined over the integers. While this discussion generalizes to an arbitrary number of dimensions, we only really need two.

We can project the Euclidean space into the index space by using the componentwise floor function

$$\downarrow \begin{bmatrix} x^{\mathrm{x}} \\ x^{\mathrm{y}} \end{bmatrix} = \begin{bmatrix} \lfloor x^{\mathrm{x}} / l^{\mathrm{cell\,x}} \rfloor \\ \lfloor x^{\mathrm{y}} / l^{\mathrm{cell\,y}} \rfloor \end{bmatrix}. \tag{134}$$

We can also inject the index space into the Euclidean space by using the componentwise shifting function

$$\uparrow \begin{bmatrix} x^{\mathrm{x}} \\ x^{\mathrm{y}} \end{bmatrix} = \begin{bmatrix} l^{\mathrm{cell\,x}}(x^{\mathrm{x}} + 1/2) \\ l^{\mathrm{cell\,y}}(x^{\mathrm{y}} + 1/2) \end{bmatrix}. \tag{135}$$

While $\downarrow$ and $\uparrow$ are not inverses of each other, they do satisfy the generalized inverse property, that is, $\downarrow \circ \uparrow \circ \downarrow = \downarrow$ and $\uparrow \circ \downarrow \circ \uparrow = \uparrow$.

In order to measure distances in the index space, it is more natural to use the Chebyshev metric than the Euclidean metric. For the sake of consistency with equations 63 and 64, we express it in terms of the particles i and j as

$$d_{i,j} = \max\{\downarrow x_j^{\mathrm{x}} - \downarrow x_i^{\mathrm{x}}, \downarrow x_j^{\mathrm{y}} - \downarrow x_i^{\mathrm{y}}\}. \tag{136}$$

We also want to use the index space to impose an order on the particles, such that we can efficiently partition them into two groups. This is best accomplished with the lexicographical order

$$\begin{cases} x_i > x_j, & \downarrow x_i > \downarrow x_j \\ x_i > x_j, & \downarrow x_i = \downarrow x_j, i > j \\ x_i = x_j, & \downarrow x_i = \downarrow x_j, i = j \\ x_i < x_j, & \downarrow x_i = \downarrow x_j, i < j \\ x_i < x_j, & \downarrow x_i < \downarrow x_j. \end{cases} \tag{137}$$

We can finally formalize the statement that particle i may only interact with particle j when $x_i < x_j$ and $d_{i,j} \leq 1$.